Revised version 2 - Manuscript prepared for American Mineralogist

Diagenetic formation of interlayer-deficient fluorophlogopite as a clay mineral in Early Cambrian phosphorite (Lesser Himalaya, India): The trioctahedral analogue of illite

GERHARD FRANZ[1)], DOROTHEE HIPPLER[1)], DIETER RHEDE[2)], RICHARD WIRTH[2)], DHIRAJ MOHAN BANERJEE[3)], NICOLAJ MAHLSTEDT[2)]

[1)]Fachgebiet Mineralogie-Petrologie, Techn. Universität Berlin, Ackerstr. 75, D 13355 Berlin, Germany

[2)]Deutsches GeoForschungsZentrum Potsdam, Telegrafenberg, D 14473 Potsdam, Germany

[3)]Department of Geology, Chattra Marg, University of Delhi, Delhi-110007, India

ABSTRACT

The occurrence of a trioctahedral analogue of illite, the dioctahedral interlayer-deficient K-mica, has long been debated. Due to the inherent difficulties of determining structure and chemical composition of the extremely fine-grained material, earlier descriptions based on separated material are equivocal. Here we describe low-temperature (diagenetic) formation of fluorophlogopite, which is interlayer-deficient and therefore analogous to illite, using high-resolution in-situ methods (transmission electron microscopy TEM, with preparation by focused ion

beam milling, combined with wave-length dispersive analysis by field-emission gun electron microprobe). The average composition is $K_{0.5}Mg_{2.8}V_{0.01}Fe_{0.005}[Si_{3.15}Al_{0.85}O_{10}(OH)_{0.65}F_{1.35}]$, including minor amounts of NH_4 for charge compensation as determined by electron energy loss spectroscopy. The K-deficient Mg-mica occurs in layer packages of ~10 layers, and no indications for interlayering with other sheet silicate layers such as chlorite or vermiculite could be identified with TEM. X-ray powder diffraction patterns of separated material confirm the absence of smectite components.

The mineral was identified in phosphorites from the lowermost Cambrian Tal Group, Mussoori Syncline, Lesser Himalayas, India. The rocks are alternating phosphatic mudstones and phosphatic dolostones, at times interbedded with phosphate-poor carbonate layers, which are rich in organic matter. Sedimentary fluorophlogopite occurs in both rock types and in two textural associations; one in vesicles filled with amorphic organic matter, the other as reaction rims around illite, which contains up to 5 wt% V_2O_3 in its rims. Textural arguments favor an early diagenetic formation of both, V-bearing illite and fluorophlogopite, closely associated with organic matter and linked to dolomitization. The high F-content stabilizes phlogopite to low temperatures. Our findings confirm that the stability field of fluorophlogopite extends from magmatic to metamorphic and sedimentary conditions.

Keywords: sediment petrology, mineral, fluorophlogopite stability, organic matter, dolomitization

INTRODUCTION

Illite, one of the most abundant clay minerals, is referred to as a non-expanding, dioctahedral, aluminous, K-bearing 2:1 sheet silicate mineral of the mica group, which has ionic substitutions in both the octahedral and the tetrahedral sites and an interlayer charge between 0.8 and 0.6 (Srodón and Eberl, 1984; Meunier and Velde, 2004) and commonly occurs in the clay-size fraction (< 2 μm). It is classified as "dioctahedral interlayer-deficient mica" by Rieder et al. (1998) and Fleet (2003) or as "hydromica" (Strunz and Nickel, 2001; Guggenheim et al., 2006), which distinguishes it from muscovite; from a petrological point of view it can be considered as "sedimentary-diagenetic muscovite". Chemically it can be described as intermediate between pure muscovite and pyrophyllite with approximately 0.65 K pfu and 3.35 Si pfu (Fleet, 2003).

The occurrence of a trioctahedral analogue of illite is debated. Rieder et al. (1998), Fleet (2003) and Guggenheim et al. (2006) list only the trioctahedral interlayer-deficient Na-mica wonesite, chemically intermediate between the Na-biotite preiswerkite and talc, as such a species. A K-bearing trioctahedral illite would thus be chemically intermediate between phlogopite respectively biotite (depending on Fe-content) and talc. Strunz and Nickel (2001) list 'hydrobiotite' and 'hydrophlogopite' (Clarke, 1895) as similar to biotite, with K-OH partly replaced by H_2O-H_2O, but 'hydrobiotite' was already redefined as a regular interstratification of vermiculite and biotite (Brindley et al., 1983).

From a petrological point of view a trioctahedral analogue of illite as a neoformation in a sediment would be a "sedimentary-diagenetic biotite", but it is a well known fact in metamorphic petrology that the biotite-in reactions

chlorite + K-feldspar = biotite + muscovite + quartz + H_2O

and

muscovite + ankeritic dolomite + quartz + H_2O = biotite + calcite + chlorite + CO_2,

occur at metamorphic greenschist facies conditions (e.g. Spear, 1993; Ferry, 1976) at 300 to 400 °C; the formation of biotite at sedimentary conditions is therefore unlikely.

However, the term 'trioctahedral illite' is used in the literature since Walker (1950), who reported trioctahedral illite in soil clays from Scotland, based on the position of the (060)-peak in X-ray powder diffraction diagrams. At these times, no chemical composition of the fine-grained material, which occurs together with weathered biotite and vermiculite, could be made, so the designation of trioctahedral illite was equivocal and Walker (1950) stated that "…it is not proposed to introduce a new mineral name at this time, since it is felt that this would be likely merely add to the existing confusion in the nomenclature of the clay micas…". Since then, there are many references describing "trioctahedral illite" as a weathering product of biotite, e.g. Soveri (1956), Wilson (1967), Fordham (1990), Burkins et al. (1999) and Persson and Olsson (2000). Parnell (1983) related the formation of trioctahedral illite in mixtures with vermiculite to the very low pH, caused by the simultaneous weathering of sulfides. New formation of "trioctahedral illite" by a reaction of early weathering products of biotite (biotite/vermiculite and vermiculite) with K-bearing solutions was proposed by Nettleton et al. (1973). In addition to weathering products of biotite, "trioctahedral illite" was applied to material from sediments, where both weathering of detrital material as well as new formation during diagenesis must be considered, e.g. in deep sea sediments by Sato et al. (1965), who reported non-swelling "trioctahedral illite" together with chlorite, kaolinite and montmorillonite from the clay fraction of rocks with a high amount of detrital material, based on XRD and

using the high ratio of the 10 Å/5 Å reflections. Clauer (2011) in a study about the significance of K-Ar-age determinations on clay minerals in Lower Cambrian, Cretaceous and Miocene sediments also used the term, but clearly stated that all the material has expandable illite-smectite mixed layers between 30 and 100% and describes "trioctahedral illite" as "… particles or particle domains in dioctahedral particles present in the illite mixtures" or "…such trioctahedral 'defects' in dioctahedral crystal structures…".

Lee et al. (1984) used high-resolution transmission electron microscopy (HRTEM) to describe the exact nature of mixtures between dioctahedral and trioctahedral layers in illitic material from rocks transitional from mudstone to slate. They and many other studies have confirmed that both random and regular mixed layers as well as packages of trioctahedral layers (mostly chlorite) and dioctahedral illite exist from the submicroscopic scale of ~100 nm to the microscopic scale of several μm, and argue that only TEM in combination with analytical TEM can clearly distinguish between the different minerals. In summary, none of the references above, where the term "trioctahedral illite" was used, unequivocally identified the true trioctahedral nature of the interlayer-deficient mica mineral.

Here we describe K-deficient fluorophlogopite, truly trioctahedral and non-expandable as a neoformation in Early Cambrian phosphorite from Lesser Himalaya, India using HRTEM on samples prepared by the focused-ion-beam (FIB) technique in combination with wavelength dispersive (WDS) and energy dispersive (EDS) electron microprobe analysis (EMPA) and XRD data. The TEM images clearly show, that there are no interstratifications with other than 10 Å layers, and the in-situ analysis yielded an average composition of $K_{0.5}Mg_{2.8}V_{0.01}Fe_{0.005}[Si_{3.15}Al_{0.85}O_{10}(OH)_{0.65}F_{1.35}]$,

including minor amounts of NH_4, which compensates the interlayer charge. The high F content stabilizes the phlogopite.

GEOLOGICAL SETTING AND SAMPLE MATERIAL

Fluorophlogopite was found in the phosphate-carbonate matrix of organic-rich phosphorites from the Mussoorie Syncline in the Lesser Himalaya, India (Banerjee et al., 1986; Mazumdar and Banerjee, 2001). The stratigraphic succession in this syncline starts with Mesoproterozoic slate and quartzite, followed by Neoproterozoic glacial diamictite, a thick argillite succession of Infra-Krol and terminal Neoproterozoic Krol Group, which mainly consists of shallow-marine dolostones, limestone, red and gray shales, all indicating deposition in a shallow marine environment. The top-most argillaceous dolomitic formation of the Krol Group is overlain by bedded cherts, black shales and pyrite-bearing phosphorites of the Lower Tal Formation (Chert-Phosphorite Member; Banerjee et al., 1997; Mazumdar and Banerjee, 2001). Black shales within this unit with well-defined light carbon isotopes (Banerjee et al., 1992) gave Re-Os isochron ages for the Precambrian-Cambrian (554±16 Ma and 552±22 Ma; Singh et al., 1999), and paleontological evidence (Brasier and Singh, 1987; Tiwari, 1999; Mazumdar and Banerjee, 1998) suggests Nemakit–Daldynian to Early Tommotian age. The Chert-Phosphorite Mb. is followed upward in the succession by marly to arenaceous member of arenites and microbial laminites of the Upper Tal Formation.

The samples studied here were collected from two limbs of the Mussoorie Syncline, Maldeota (= MA) located in the southern limb and Durmala (= DUR) on the northern limb; for localities and detailed stratigraphy, see Banerjee et al. (1997), Mazumdar and Banerjee (2001) and Brasier and Singh (1987). The Chert-Phosphorite

148 Mb. consists of phosphatic beds of variable thickness, with the main phosphate unit
149 reaching total thicknesses of up to 10 m in some places (Banerjee, 1986). The
150 phosphorites mainly show mudstone or pelletal fabrics, as well as brecciated
151 mudstone fabrics. The rocks are brittle deformed with no signs of metamorphism.
152 For the mineralogical characterization of the phosphorites, we selected 12
153 samples based on our experience from a large suite of samples, which show the
154 representative variation in macroscopic structures. Visible alteration is limited to very
155 narrow rims of Fe-oxide-hydroxide around pyrite near the surface of the samples.
156 Fluorophlogopite was identified in brecciated phosphatic mudstones-dolostones
157 (samples DUR-7, DUR 11, DUR 15, MA-4), with sample DUR-7 described in detail
158 below (see Results). The other samples from Durmala are phosphatic stromatolite
159 (DUR-11) and DUR-15 contains phosphatic oncoids and pyrite-rich layers. The
160 sample from Maldeota (MA-4) is a phosphate-bearing granular dolostone or dolo-
161 grainstone, with small pieces of brecciated phosphatic mudstone.
162 For the characterization of the organic material with total organic carbon (TOC)
163 content and Rock-Eval analysis we used two samples from each locality (phosphatic
164 dolomite-rich mudstone DUR-9; phosphatic mudstone with a pyrite layer DUR-15
165 split into the phosphatic layer DUR-15a, the pyrite layer DUR-15b and mixed
166 material DUR-15rest; phosphatic mudstone MA-5; phosphatic layer separated from
167 grey dolostone MA-10c).
168
169 **METHODS**
170 XRD data were obtained on non-oriented powder from the whole rock, using a
171 Bruker D2 Phaser instrument with Cu-Kα radiation at 30 kV/10mA; fixed divergence
172 slit 1.0 mm; graphite monochromator; step size 0.002 °2Θ; 2.0 s/step; measured from

5-75 °2Θ. Oriented patterns were obtained with a Philips instrument, Cu-Kα radiation, from the fraction < 2 µm, which was separated after crushing the rock to < 63 µm, shaking in distilled water for several hours and dispersing it with sodium-pyrophosphate.

Electron microprobe analyses (EMPA) were obtained with a Jeol JXA-8500F instrument equipped with a field emission cathode, first using the standardless energy dispersive (EDS) mode, then on selected crystals the wave-length dispersive (WDS) mode with an acceleration voltage of 10 kV and a sample current of 10 nA. For a one µm wide beam the calculated penetration depth is approximately 1.5 µm on an area slightly larger than one µm in diameter. Apatite was analyzed with a beam diameter of 5 µm. Standards were albite (Na), orthoclase (K, Si, Al), Fe_2O_3 (Fe), apatite (P), rhodonite (Mn), MgO (Mg), fluorite (F), pure V. Crystals for analysis and counting times on peak respectively back ground were PET for K, Ca (20/10 s), P, V (30/15); TAP for Si, Na, Mg, Al (20/10); LiF for Fe, Mg (30/15); LDE for F (30/15). Detection limits and standard deviation (one sigma) at these conditions are approximately 200 ppm/20 % for Na, 800 ppm/10 % for Fe, 250 ppm/2 % for K, 250 ppm/0.5 % for Si, 250 ppm/25 % for P, 900 ppm/100 % for Mn, 300 ppm/12 % for Ca, 140 ppm/1 % for Mg, 260 ppm/8 % for F, 400 ppm/15 % for V. The CITZAF routine in the JEOL software, which is based on the Φ(ρZ) method (Armstrong, 1995), was used for data processing.

Mica formulae and cations per formula unit (cpfu) were calculated assuming $O_{20}(OH,F)_4$. Chemical zoning was investigated by X-ray element mapping in WDS mode moving the stage in steps of 0.2 µm with a focused beam. A high voltage of 10 kV and a beam current of 10 nA were used. The dwell times varied from 300 to 400 ms per pixel (500*350 pixels, 380*270 pixels).

198 Transmission electron microscopy (TEM) foils were prepared using a focused ion
199 beam (FIB). Typical FIB-cut TEM foils have the dimensions 15 µm x 10 µm x 0.150
200 µm. Details of the FIB milling technique are presented in Wirth (2004, 2009). The
201 electron-transparent foils were studied in a Tecnai F20 X-Twin transmission electron
202 microscope operated at 200 kV with a field emission gun as electron source. This
203 TEM is equipped with a Gatan imaging filter GIF™ (Tridiem), a Fishione high-angle
204 annular dark field detector (HAADF) and an energy dispersive (EDAX) X-ray
205 analyzer with ultra-thin window. Bright field, dark field and high-resolution TEM
206 images are usually acquired as energy filtered images applying a 20 eV window to the
207 zero loss peak of the electron energy-loss spectrum. Energy dispersive X-ray analysis
208 was performed scanning the electron beam in the scanning transmission mode across
209 the area of a pre-selected area thus avoiding mass loss during the data acquisition.
210 Counting time was 60 to 120 seconds. Analytical data were processed using the
211 TIA™ software package. Electron diffraction data were acquired as selected area
212 electron diffraction pattern (SAED) or derived from high-resolution lattice fringe
213 images applying a fast Fourier Transform (FFT), which results in a calculated
214 diffraction pattern. This technique was applied to nanocrystals. Electron energy loss
215 spectra (EElS) were acquired in diffraction mode using a camera length of 700 mm.
216 Applying an 1 mm entrance aperture the resulting acceptance semi angle is 5 mrad.
217 Dispersion was 0.1 ev/pixel. Acquisition time was 1 second to minimize electron
218 beam damage during exposure. Data processing occurred applying the Digital
219 Micrograph™ software package.

220 Analysis of the organic matter was performed in two steps, oxidation (Leco
221 SC-632 instrument for TOC determination) and pyrolysis (conventional Rock-Eval
222 measurement using a Rock-Eval 6 instrument (Behar et al., 2001). Jet Rock 1 was

run as a standard and checked against the acceptable range given in Norwegian Industry Guide to Organic Geochemical Analyses (NIGOGA; Weiss et al., 2000). Up to 120 mg of finely crushed rock were treated with diluted HCl (1:9 HCl:H_2O) at 60°C to remove inorganic carbon, then introduced into the combustion oven operating at 1350°C. To ensure full conversion to CO_2, oxygen is purged into the oven. The amount of TOC in wt% was calculated using CO_2 concentrations measured by an infrared detector. For pyrolysis the temperature program was set to an isotherm at 300°C, held for 3 minutes followed by a heating phase with a rate of 25°C/min up to 650°C. The bulk hydrocarbons were immediately transported in a He gas flow to a flame ionisation detector. Generally, two well-defined peaks are recorded; S1 represents the amount of extractable products at 300°C which are free hydrocarbons formed up to the present maturity stage of the organic matter and still remain within the source rock, and S2 represents the phase of volatilization of the heavy hydrocarbons compounds (>C40) as well as the remaining hydrocarbon potential generated by cracking of the organic matter during heating. T_{max} is the temperature at which S2 reaches its maximum and depends on the nature and maturity of the analysed kerogen, with higher maximum temperatures for higher maturity stages. In addition, CO_2 issued from the cracking of oxygen-containing functional groups in the organic matter is trapped in the 300°-390°C range, then released and detected by thermal conductivity detection during the cooling of the pyrolysis oven producing the S3 peak which can be used as a measure for the oxygen richness of the kerogen. S1, S2 and S3 together with TOC are input parameters for the calculation of hydrogen index (HI), oxygen index (OI), and production index (PI).

RESULTS

Petrography

The specimen DUR-7 (Fig. 1) shows layering of alternating phosphatic mudstone with sparitic dolostone, in which brecciated layers of phosphorite or phosphatic mudstones are immersed in a dolomite-rich matrix. The sample is almost opaque in thin section due to the high content of organic matter, the alternating sparitic dolostone layers are translucent. The phosphatic mudstone is finely laminated on a sub-mm scale with alternating organic matter and apatite layers, with the lamination sometimes crinkled to wavy. This fabric is interpreted as former microbial mats, providing a microenvironment for early-diagenetic phosphatization at the sediment-water interface. Thin to subtle carbonate layers are interbedded between the phosphatic mudstone layers, indicating episodic onset of the carbonate factory (Schlager, 2005). The phosphatic mudstone layers are sometimes warped, disrupted or brecciated, likely as a result of in-situ reworking due to desiccation (or dewatering), storms or seismic events, and show diagenetic crosscutting veining as irregular up to 2 mm-wide veins filled with sparry dolomite and as smaller regular dolomite-filled veins perpendicular to the layering (Fig. 1).

Apatite occurs in three different textural types: (i) flocculent to pelletal fabrics with an approximate pellet diameter of 5-15 μm together with (ii) botryoidal apatite, in which single laminae are pigmented with organic matter, features of earliest diagenesis (both labeled apatite I), and (iii) homogeneous sparry apatite crystals, which are interpreted as late diagenetic recrystallized apatite II. Associated pyrite is found as spherical to sub-spherical pyrite framboids with framboid diameters varying from ~5 to 20 μm and consisting of irregularly oriented nanocrystals (Appendix Fig. 1); individual crystals with a size of ~100 to several hundred nm dispersed in

botryoidal apatite (both called pyrite I); euhedral pyrite in ~50 µm large crystals and in aggregates (pyrite II). Sphalerite was observed rarely (Appendix Fig. 1). Quartz fills irregular interstices in the phosphatic matrix, often surrounded by organic matter, with its shape excluding a detrital origin. Dolomite in the sparitic dolostone layers (Fig. 2a) and irregular veins has a variable grain size of <100 µm up to several hundred µm. It is slightly zoned with Ca-rich inner parts. Along cracks and on boundaries to organic matter it is partly replaced by calcite (Fig. 2a). Dolomite also occurs in the phosphatic mudstone layers in characteristic round to oval (possibly former organic or carbonate) structures (Fig. 2d), typically with a high porosity and in places associated with small amounts of calcite; it is found in interstices between botryoidal apatite, and in recrystallized sparry crystals. Illite in flakes of ~20 to ~100 µm (Fig. 3a) is oriented parallel to the bedding. Rutile as an accessory mineral is also found associated with the clay minerals. Organic matter, present in interstices between dolomite (Fig. 2a,b), in round to ovoid structures within the phosphatic matrix (Fig. 2d,e,f) and as nm-sized pigment throughout the rock, contains ~1 to 2 wt% S, also minor and variable amounts of Si, Ca and P, probably present as nano-scale silica and apatite inclusions.

Fluorophlogopite occurs (i) together with organic matter in vesicles and interstices between dolomite (Fig. 2a,b) and (ii) as overgrowths on illite (Figs. 3-5). Within the sparitic dolostone layer it forms aggregates of a few µm thickness and several tens of µm elongation (Fig. 2b) within organic matter, which fills the spaces between euhedral dolomite crystals. Orientation of the crystals is subparallel (Fig. 2c), organic matter is also included parallel to the layers, and very small nm-sized crystals of apatite (identified by EDS-analyses) are occasionally found. In the phosphatic matrix of the mudstone layers, ovoid vesicles ~10 x 30 µm in size are filled with

organic matter (Fig. 2d,e) and fluorophlogopite, together with illite, in irregular oriented aggregates. Here particles are << 1 μm thick and only a few μm long, concentrated at the rim and extending from the rim into the vesicle (Fig. 2e,f). Another site (Fig. 3) shows fluorophlogopite as overgrowth on illite and in a vesicle with organic matter and calcite in larger flakes (Fig. 3b).

Fluorophlogopite also forms overgrowths on illite (Figs. 3a, 4a), preferentially in the a-b direction (Fig. 4b), but also forms aggregates with quartz grains, apatite and some pyrite grains, within apatite. X-ray mapping (Fig. 4c-f) highlights three different types of mica; (i) an inner core of illite with a homogeneous appearance in BSE, surrounded by (ii) a rim of V-bearing illite, which forms layer packages oriented parallel to (001), which is surrounded by (iii) fluorophlogopite. Apatite is also rich in F (Fig. 4c). In V-bearing illite, V-contents increase systematically in growth direction from the border of the illite towards the border to fluorophlogopite (Fig. 4d). The Mg- and Al-mappings also show that the three types of mica are clearly separated from each other, and that on the resolution of the EMPA of approximately 200 nm no interlayering is visible. BSE images were used for positioning of the electron beam for quantitative analyses to avoid overlapping analysis. Only in the analysis aimed at the highest V-contents with 5 wt% V_2O_3 overlap with the K-deficient Mg-mica could not be avoided. In the sample, the V-content of illite crystals is heterogeneous, at some places V_2O_3 is below the detection limit. Rarely, an isolated flake of V-bearing illite was observed in the organic matter.

Another site of X-ray mapping shows an illite crystal with its tip of fluorophlogopite growing into dolomite with an ellipsoidal shape (Fig. 5a). For the X-ray mapping the thin section had to be repolished, and after repolishing showed the contours in Figure 5b (note different scale, larger area compared to Fig. 5a). The

extensional crack, which is visible in (a) only in the upper part of apatite, now clearly crosscuts the whole structure, including the mica and the dolomite, which has inclusions of fragmented apatite I (see Ca-Mg-distribution; Fig. 5e,g). As shown in Figure 4, apatite is also rich in F (Fig. 5c). The X-ray mapping confirms the clear boundary between fluorophlogopite and illite (Fig. 5f), and the presence of apatite in narrow layers parallel to (001) in illite (Fig. 5c,g). The extensional cracks (Fig. 5d) are filled with a Mg-sheet silicate devoid of K (Fig. 5e,f), probably chlorite. The X-ray mapping of Fe (not shown) indicates only small, homogeneously distributed amounts in illite, undetectable in all other minerals including chlorite. At this site, a V-rim (X-ray mapping not shown) around illite is missing, but we analyzed also a third site by X-ray mapping where fluorophlogopite is associated with illite and V-bearing illite.

Electron microprobe analysis

Quantitative wavelength dispersive analyses of fluorophlogopite and illite are shown in Table 1 and shown in Figure 6. Similar values were first obtained with the EDS mode, also for the other samples DUR 11, DUR 15 and MA-4 mentioned above (Table 1), however with a higher amount of FeO, and in DUR 15 the K_2O content is higher. The formulae (calculated on a basis of 22 oxygen) for fluorophlogopite are in agreement with an almost fully occupied trioctahedral F-dominated and K-deficient mica with a narrow compositional range. For illite the analyses are in good agreement with pure illite as given by Meunier and Velde (2004), although with a wider range in composition. The analysis point which clearly indicates a mixed analysis (with the strongest BSE contrast and highest V-contents) has an octahedral occupancy of 4.6 atoms pfu (Fig. 6a) higher than expected for a dioctahedral mineral. Fluorophlogopite

as well as the two illite varieties show an octahedral occupancy with average values of 4.2 and 5.7 atoms pfu respectively, which is in the normal range for di-tri-octahedral solid solution (Monier and Robert, 1986). They also show a clear deficiency in the interlayer position (Fig. 6a); K-contents are much higher in illite compared to V-bearing illite and fluorophlogopite. For Si the average value in fluorophlogopite and illite is is 6.3 and 6.45 pfu, respectively, but the variation is much larger for illite (Fig. 6b). Octahedral Al in fluorophlogopite is small around 0.15 pfu, in illite it varies between ~2.7 and 3.9 pfu (Table 1). Comparison between Fe and Mg (Fig. 6c) again shows the difference between the three micas: fluorophlogopite and V-bearing illite have very low Fe contents, whereas illite is variable, with up to 0.8 Fe pfu. Vanadium as a minor or trace element is present in V-bearing illite with up 0.45 pfu (5 wt% V_2O_3), In fluorophlogopite and in the normal illite it is present with $\leq$ 0.05 pfu (Fig. 6d). The negative correlation with ^{VI}Al indicates a V^{3+} valence state and substitution in the octahedral layer; the deviation from the 1:1 reference line towards smaller Al-contents is due to the Si-Al-variation in illite. Fluorine is also an element, which allows distinguishing fluorophlogopite from illite (Fig. 6e); it varies between 2.5 and 3 pfu, i.e. much more than 50 mol% of the F-endmember. In illite and V-bearing illite it is mostly below ~ 0.5 pfu.

X-ray powder diffraction

Powder diffraction patterns of un-oriented whole rock powder as well as the separated fraction < 2 µm in an oriented sample show (next to F-apatite, dolomite, calcite, quartz) a (00l) mica peak. The separated fraction < 2 µm was treated with ethylene glycol and tempered at 550°C; XRD powder diagrams do not differ after treatment and there is no indication for smectite in the whole sample or a smectite

component in the micas (Appendix Fig. 2). The whole-rock powder was treated with H_2O_2 to oxidize the organic matter and slightly with CH_3COOH to remove some carbonate (however, calcite and dolomite were still present). The (060) peaks for both, di- and trioctahedral micas at ~61.9 and ~60.16 °2θ (Moore and Reynolds, 1989) are present (Appendix Fig. 2).

Transmission electron microscopy

Two FIB-foils were cut, one from the sparry dolomite layer within organic matter (Fig. 7), one from the site within the phosphate matrix (Fig. 8). The HAADF image (Fig. 7a) and bright field imaging of the site in the dolomite layer (Fig. 7b,c) shows the parallel orientation of the crystals. Individual areas with homogeneous contrast indicate thickness of 30 to 50 nm for layer packages. Porosity as lenticular voids is oriented parallel to the cleavage planes, ≤50 nm wide and several hundred nm long (Fig. 7b). The phase boundary is ~30 nm wide (Fig. 7c). High-resolution imaging of fluorophlogopite and selected area diffraction pattern (Fig. 7d) shows individual layer packages of 7 to 13 layers, and each layer is 10.1 Å thick. There is no indication for other trioctahedral Mg-rich layers. Packages are separated by low-angle grain boundaries, are tilted in the b-c-plane and show stacking faults. Organic matter shows a slight structural organization (Fig. 7e) in a high-resolution image of the interface to fluorophlogopite and weak rings in the selected area diffraction pattern. Over a width of ~20 nm, organic matter is completely amorphous.

At the site in the apatite layer, fluorophlogopite and illite are irregularly distributed within organic matter (HAADF and bright field imaging; Fig. 8a,b). Packages of fluorophlogopite and illite, distinguished by analytical TEM (Fig. 8d-f) are several hundred nm long and are very variable in thickness. Short-prismatic

apatite crystals are in the order of 30 x 60 nm in size. The interface apatite-organic matter with mica shows a slight porosity; nm-scale pores where also found within apatite and within organic matter further away from the boundary (Fig 8b). Although the BSE image indicated growth of the mica from the rim into the ovoid vesicle (Fig. 2e), the TEM images show that growth of mica and apatite is not related by any structures such as an overgrowth or epitaxial orientation. Dark field imaging (Fig. 8c) also reveals the small size of mica crystals at the border between apatite and organic matter.

Analytical TEM with EDAX confirmed the results obtained by EMPA. Fluorophlogopite is dominated by Mg, is mostly Fe-free or shows only a small Fe-peak and is rich in F; at the site within apatite (see Fig. 2d,e and Fig. 7) it has a small and variable content of V. EDS analysis (Fig. 8d,e,f) allows distinguishing flouorophlogopite from illite by their Al/Mg. From two areas, EELS data were obtained (Fig. 9). The spectra confirm the high amount of F (Fig. 9c), but show also small amounts of NH_4^+ (Fig. 9a,b).

Characterization of organic matter

The samples (and fractions) from Durmala exhibit TOC contents of ~1 wt% whereas the phosphatic mudstone sample from Maldeota is organic richest with a TOC content of 2.2 wt% (Table 2). The dark phosphatic layer from the latter locality shows the lowest TOC content. Based on very low S2 respectively HI values (<1 mg HC/g sample respectively <10 mg HC/g TOC) and unreliable T_{max} values <415 °C, all samples can be described as thermally overmature. Because T_{max} is maturity dependent, T_{max} values should increase from ~420 °C to higher temperatures with maturity. The here observed low values are caused by the extremely low amounts of

hydrocarbons generated upon pyrolysis (high maturity) inducing a low signal to noise ratio of the S2 trace, which hampers a meaningful T_{max} assignment. Because S1 is near zero, calculation of the production index is also not meaningful.

DISCUSSION

The combined data – XRD from the fine fraction of the whole rock, EMPA and TEM – clearly identify fluorophlogopite. XRD confirms that there are neither smectite components in the mica nor smectite minerals in the rock. HRTEM images confirm the regular 10 Å-spacing, with no indications for other sheet silicates as interlayers. The quantitative chemical analysis (WDS; Table 1) yielded an average formula of $K_{0.5}Mg_{2.8}V_{0.01}Fe_{0.005}[Si_{3.15}Al_{0.85}O_{10}(OH)_{0.65}F_{1.35}]$ based on a general formula $I_{1.0}M_{3.0}[T_{4.0}O_{10}(OH,F)_{2.0}]$ for mica, with a generally small scatter between the individual analysis points taken from different parts of different crystals in the thin section. Although the EDS data obtained from the other localities (Table 1) are of much poorer quality they are sufficient to characterize the micas as very similar to that of the sample DUR7. The sum of the determined oxides (wt%, corrected for F) from the WDS analyses is 97.4 wt%. Because the (OH)-position is mainly filled by F and only 1.3 (OH) pfu, the amount of H_2O which has to be added to the analysis is in the order of 2-3 wt%; keeping in mind that fluorophlogopite has also intergrowths of organic matter and some NH_4^+ the analyses are close to a sum of 100 wt%. NH_4^+, present in small amounts as indicated by the weak but clearly identifiable peak in EELS (Fig 9b), is commonly considered as part of the interlayer and would thus add to the 0.5 K pfu. However, calculations assuming different amounts of NH_4 pfu show that above 0.25 wt% NH_4 (equivalent to 0.28 pfu) the formulae turn out to be poor in quality concerning charge balance and occupation of < 4.0 for the tetrahedral layer.

448 The interlayer is therefore occupied with max. 0.7 pfu. Notable is the high F content
449 in all analyses (Table 1, Fig. 5e) with more than 50 mol% of the F endmember.
450 Small amounts of Ca and P (< 1 wt% each) were identified in most analyses.
451 Very likely they are due to the presence of small apatite inclusions (see Fig. 2c), but it
452 cannot be excluded that part of the P substitutes for Si, and that Ca is present in the
453 interlayer. In any case, these amounts are minor.
454 The accompanying illite is similarly interlayer-deficient, and the analyses also do
455 not indicate the presence of other sheet silicates interlayered into illite. Its large grain
456 size indicates a detrital origin, probably formed from muscovite. The main difference
457 to fluorophlogopite (in addition to the di-octahedral Al- versus trioctahedral Mg-
458 occupation) is the variable and high Fe-content, the larger variation in Si in the
459 tetrahedral sheet, and the low F content. The V-bearing variety of illite has like
460 fluorophlogopite no Fe, but higher F-contents than normal illite.
461 In addition to the fact that fluorophlogopite is K-deficient and therefore a
462 trioctahedral Mg-analogue of illite, there are more similarities. Meunier and Velde
463 (2004) describe illite as a mineral that mostly occurs in the clay fraction; in the
464 phosphorite fluorophlogopite is clearly part of the clay fraction, with crystal sizes
465 down to the nanometer scale (Fig. 2, especially e,f; Figs. 7,8). Illite is commonly
466 found in layer packages of ~ 10 layers per package, which was also observed in our
467 samples (Fig. 7d). Finally, Meunier and Velde (2004) also state that minor amounts of
468 NH_4 are typical for illite; the NH_4-content in the fluorophlogopite is ascribed to
469 bacterial or thermal degradation of organic matter, with which it is closely associated.
470 In many occurrences illite is present in mixed-layered minerals (ordered or
471 disordered) together with an expandable smectite component, vermiculite, chlorite or
472 other sheet silicates, and such material is referred to as ‘illitic material’ (see review by

Srodón and Eberl, 1984; Moore and Reynolds 1989) and most references of "trioctahedral illite" refer to such material. However, there are indications for the existence of previously described trioctahedral analogues of illite. From the metamorphic graphite deposit Kropfmühl, Bavaria (Germany) Weiss et al. (1956) described brownish, earthy material which contains silver-white to slightly red-brownish aggregates of what they called trioctahedral illite together with batavite, vermiculite and biotite. They determined the mica structure by single-crystal methods (Weißenberg and Laue camera) and the composition by wet chemistry as $K_{0.66}(Mg_{2.93}Al_{0.06})_{2.99}[Al_{0.70}Si_{3.30}O_{10}|(OH)_2]$, a Mn-rich variety as $K_{0.67}(Mg_{2.26}Mn_{0.64}Al_{0.11})_{3.01}[Al_{0.84}Si_{3.16}O_{9.98}|(OH)_2]$ and an Fe-rich variety as $K_{0.67}(Mg_{2.62}Fe_{0.24}Al_{0.12})_{2.98}[Al_{0.99}Si_{3.01}O_{10}|(OH)_2]$. They argued that the vacancies in the interlayer are partly occupied by water molecules according to their water determination; the mineral was not expandable with water, ethylenglycol or glycerin, but exchanges K for alkyl-ammonium and was clearly distinguished from the accompanying other trioctahedral 2:1 layer silicates. Comparing the K-deficient fluorophlogopite from the phosphorites to the data given by Weiss et al. (1956), the Si content is significantly higher in the mica from the phosphorites, and unfortunately Weiss et al. (1956) did not report F. In metasomatic talc zones around serpentinites intruded into sedimentary rocks from Hokkaido, Japan, Ushizawa (1981) identified "trioctahedral illite" together with chlorite by XRD, DTA and wet chemical analysis. The given composition is $K_{0.51}Na_{0.05}(Mg_{1.87}Fe_{0.37}Al_{0.63})_{2.87}[Al_{0.95}Si_{3.05}O_{10}|(OH)_2]$. Deocampo et al. (2009) described clay minerals from a saline lake with an intermediate octahedral occupancy of ~2.5 ($Al_{0.09}Fe_{0.23}Mg_{2.09}$), based on combined HRTEM, XRD and infrared data, possibly consisting of di- and trioctahedral domains or alternatively as homogeneous di-trioctahedral sheets. The importance of reactions

498 with an ambient fluid for the formation of the K-deficient Mg-mica is stressed by
499 Bodine and Loehr (1979), who described the formation of a trioctahedral mica clay
500 mineral as due to contact metamorphism between basaltic dykes, intruded into salt
501 deposits. The mica was determined by XRD and chemically characterized as
502 phlogopite with a significant interlayer-deficit stoichiometry and a Si:Al ratio slightly
503 higher than 3:1. The authors suggested formation from K-rich brines reacting with
504 talc and corrensite-rich clay assemblages, in contrast to the occurrence in the
505 phosphorites, where the fluid must be Mg-dominated.
506

507 **IMPLICATIONS**

508 Formation of illite is generally associated with (i) loss of K during leaching of
509 muscovite and/or K-feldspar (inheritance; e.g. Heiman, 2010); (ii) by transformation
510 through the addition of K (aggradation) to montmorillonite and/or kaolinite; or (iii) by
511 neoformation involving precipitation from solutions. The data show that
512 fluorophlogopite in the phosphorite is neither detrital nor a weathering product of
513 former biotite, as in many other descriptions of 'trioctahedral illite' (see references
514 above). It was formed within the sediment and within organic matter, which is
515 amorphous with only very weak ordering (see Fig. 7e), and therefore metamorphic
516 conditions are unlikely. The preserved small grain size of apatite I, and the
517 nanocrystals of pyrite I in the framboids also indicate minor diagenetic
518 recrystallization. However, larger sub- to euhedral crystals of apatite II and pyrite II
519 prove a progressive diagenetic history, but it is uncertain which conditions were
520 reached. Nevertheless, the formation of fluorophlogopite in vesicles of apatite I
521 together with organic matter point to a very early formation. Degradation of the
522 organic matter produced NH_4 and also liberated V, incorporated mainly into illite and

523 fluorophlogopite in small amounts. Diagenetic formation is also shown by its
524 occurrence interstitial between sparitic dolomite (Fig. 2a-c) and by its intergrowth
525 with dolomite (Fig. 5a). The fluids, which caused the dolomitization, likely also
526 produced fluorophlogopite and it can be speculated that a high concentration of Mg
527 (derived form seawater, seawater-modified or admixed porewaters or meteoric
528 waters) in the brines is responsible for the formation. Seawater was probably also the
529 source of F as observed in modern phosphorites (e.g. Froehlich et al., 1988), which
530 diffuses into the porewater.

531 In contrast, the much larger grain size of illite, its parallel orientation to the
532 layering of the phosphatic mudstone and the chemical variability, especially in Fe
533 compared to fluorophlogopite may either point to a detrital origin, with platy illite
534 crystals oriented during deposition of the mudstone layers, or to an authigenic
535 formation as direct precipitate or from a precursor clay mineral. Difficulties thereby
536 arise in the differentiation between detrital illite and the presence of discrete illite, so-
537 called authigenic illite (Meunier and Velde, 2004). Illite has small lamellae of apatite
538 parallel to its cleavage plains (see Ca-distribution in Fig. 5g), which is also an
539 indication that it formed prior or syngenetic to phosphate in the sediment. The illite
540 reacts with the dolomitizing fluid, supplying both Mg^{2+} and CO_3^{2-} for dolomite and in
541 a first stage V and Mg to form V- and Mg-rich illite, then fluorophlogopite as
542 overgrowths. The sharp contrast between Mg-rich and Al-rich zones excludes
543 mixtures or transitions between the illite and fluorophlogopite.

544 Textural arguments and element distributions (Fig. 5) again point to formation of
545 fluorophlogopite linked to dolomitization at a very early stage of diagenesis. The
546 extensional crack (Fig. 5b,d) approximately perpendicular to the layering crosscuts
547 illite-fluorophlogopite, dolomite as well as fragmented botryoidal apatite I in the

548 dolomite. Within the mica it is offset into several parts parallel to the basal plane
549 (001) and filled with a sheet silicate, probably chlorite (Fig. 5d,e). Cracking of the
550 mica as a result of extension during compaction shows that it was formed early during
551 compaction.

552 The trioctahedral Mg-rich analogue of illite is rare due to the fact that below the
553 biotite-in isograd the alternate common sedimentary or early diagenetic assemblage is
554 illite + chlorite + K-feldspar + dolomite + quartz. This raises the question, why it
555 occurs in the phosphorite sediments. It is well known that exchange of F for OH in
556 phlogopite extends its stability field (e.g. Ginafagna et al., 2007). Therefore it is stable
557 at atmospheric pressure, but melts at 1390 °C (Shell and Ivey 1969) and can occur in
558 lava vesicles from Mt. Etna, together with fluorapatite (Gianfagna et al. 2007;
559 Scordari et al. 2013). Obviously, F-substitution for OH also extends the stability limit
560 to much lower temperatures than those of the common biotite-in isograd.

561 It is clear that the pore fluid, from which it precipitated, must have been very rich
562 in F, which is also indicated by the presence of F-apatite. This is likely the case for
563 many phosphoritic sediments, because (carbonate) F-apatite is the common phosphate
564 mineral, and phosphorites generally contain a few wt% F (e.g. Trappe, 1998). It is
565 also known that among the OH-bearing phases involved in the biotite-in reactions,
566 biotite strongly fractionates F, very pronounced for Mg-rich compositions (see review
567 by Fleet, 2003), which is the case for fluorophlogopite in the phosphorites.
568 Application of the geothermometer of Zhu and Sverjensky (1992), which is based on
569 the empirical calibration of the F-OH partitioning between biotite and apatite is
570 impossible, because of unknown amounts of CO_3 and OH in apatite (note the nano-
571 scale inclusions of organic matter in apatite) and the known problems in analyzing F
572 in apatite by EMPA (Pyle et al., 2002). In addition, at high $X_F^{apatite}$ the calculated

573 temperatures would be very sensitive to the absolute amounts of F-OH in apatite.
574 Another possibility to estimate temperatures of formation would the method of
575 Battaglia (2004), which is based on the interlayer deficiency of illite and its Mg-Fe
576 contents. Using this T-equation for the average illite analysis (Table 1) yields 225 °C;
577 however, these temperatures vary extremely due to the large variations in K, Fe and
578 Mg of individual analyses of illite in the phosphorite. In addition temperatures are
579 likely overestimated by ~50°C (Bourdelle et al., 2013; their Fig. 5).

580 Based on our data it is neither possible to clearly define the maturity of the
581 organic matter nor to determine the origin of the organic matter. The very low "rest"
582 genetic HC potential is indicative of a more or less complete conversion of organic
583 matter into hydrocarbon gases and hydrogen-poor residue (which is present in the
584 samples as illustrated by aromatic stacks in amorphous organic matter in the TEM
585 pictures) which might in turn be indicative of a minimum geologic temperature the
586 organic matter might have experienced. Assuming the organic matter is not inertinite
587 (low HC potential at low maturities; but inertinite would not appear amorphous in the
588 TEM pictures) but rather pyrobitumen (organic matter is rather filling pore spaces
589 than appearing as single macerals, see Figs. 2 and 3) derived from the cracking of "oil
590 or bitumen", a minimum temperature of ~200 °C can be deduced. Cracking of in-
591 source oil to gas, i.e. oil retained in the source rock, was shown to most likely proceed
592 between 150 and 200 °C (e.g. Dieckmann et al., 1998), whereas in-reservoir cracking,
593 i.e. migrated oil, proceeds at higher temperatures between 170 and 240 °C (Schenk et
594 al., 1997) (temperature ranges are valid for a geologic heating rate of ~5 K/Ma;
595 slower heating rates would imply cracking at lower temperatures). Case studies have
596 shown that in coal-bearing sediments NH_4-bearing illite forms during anthracite
597 formation at 200 – 275 °C (Daniels and Altaner, 1990; Daniels et al., 1994).

598 Considering the almost amorphous nature of the organic matter and the high maturity
599 in the geological context of the area, we assume that maximum temperatures were
600 around ~200 °C.

601 In summary, the sequence of events is as follows: Deposition of the Lower Tal
602 black shale-chert-phosphorite succession occurred in a protected anoxic lagoonal
603 basin dominated by episodic upwelling of organic-rich anoxic waters to the coastal
604 flats (Banerjee et al., 1986; 1997; Mazumdar and Banerjee, 2001). Thermal and/or
605 anaerobic degradation of organic matter, notably during bacterial sulfate reduction by
606 prolific populations of bacterial sulfate reducers (i.e. 2 $CH_2O + SO_4^{2-} \rightarrow H_2S + 2$
607 HCO_3) released amongst others P, CO_2 and minor amounts of NH_4 and V to the
608 interstitial waters. Effective shuttling and thus concentration of P within the porewater
609 allows phosphogenesis to occur at the water-sediment interface. Mediating activity of
610 sulfate-reducing microbiota is evidenced by the conspicuous pyrite and sphalerite
611 mineralization. Syngenetic illitization in the presence of precursor clay minerals
612 and/or K-feldspar or the deposition of detrital illite (muscovite) is also evident, as
613 well as the episodic onset of the carbonate factory (Schlager, 2005) leading to the
614 deposition of fine to subtle carbonate layers. Syndiagenetic warping and brecciation
615 of phosphatic layers, likely as a result of hydraulic fracturing and as seen in the
616 handspecimen (Fig. 1a) predates dolomitization, which also happened during early
617 diagenesis: Precipitation of apatite depends on Ca/Mg in the fluid, and requires values
618 >5.2 at pH 7.5 to 8 (see review by Knudsen and Gunter, 2002). When apatite
619 precipitates from pore water, this reduces Ca and calcite can then react with Mg-rich
620 pore fluid to dolomite.

621 If (authigenic or detrital) K feldspar was already present (speculative) the
622 fluorophlogopite could have formed according to the equilibrium (written for the

623 interlayer-deficient endmember with 0.5 K, 2 F pfu)

624 3dolomite + 0.5K-feldspar + $2SiO_2$ + 2HF = fluorophlogopite + 3calcite + $3CO_2$ +

625 H_2O.

626 However, there are no indications for relict K-feldspar, whereas textures indicate
627 direct precipitation of the fluorophlogopite from fluid(s) in pore space with the
628 appropriate composition, hydrous with a very small X_{CO2} as deduced from the
629 position of the biotite-forming reactions at elevated *P-T*-conditions, but with a very
630 high X_{HF}, a high Mg-content and NH_4 from degradation of organic matter. A low
631 X_{CO2} could have been achieved by preceding precipitation of carbonate-fluorapatite
632 and dolomite, trapping CO_2. It is uncertain what types and amounts of hydrocarbons
633 (X_{CH4}) were present, either as a separate phase or dissolved in the hydrous phase.
634 Where illite is present, it could react with the pore fluid and we observe that first V-
635 illite is formed, with V provided by the organic decay, then the fluorophlogopite.
636 Continuous compaction likely during burial diagenesis caused extensional cracks,
637 which are filled with chlorite. The observation of de-dolomitization in the form of
638 small calcite rims around dolomite (Fig. 2a,b) may also be related to this later stage of
639 diagenesis.

640 Our findings confirm the occurrence of a trioctahedral sedimentary-diagenetically
641 formed mica, with similar properties as illite concerning crystal size, layer packages,
642 interlayer deficiency and the substitutions in the tetrahedral-octahedral layers. Mg-
643 rich trioctahedral mica of the solid solution series phlogopite-fluorophlogopite with
644 its well-known common occurrence in metamorphic-metasomatic marbles from a
645 wide range of *P-T* conditions (Fleet 2003) therefore has an extremely wide range of
646 stability, at atmospheric pressure from sedimentary-diagenetic to volcanic, at high
647 pressure up to upper mantle conditions.

ACKNOWLEDGEMENTS

This work is part of the Research Group 736 "The Precambrian-Cambrian Biosphere (R)evolution: Insights from Chinese Microcontinents" of the German Science Foundation, Grant # DFG FR 557-22/1 and HI 1553/1-2, and we are grateful for support as well as many lively discussions among the members of the research group; DB acknowledges support from the Alexander-von-Humboldt Foundation for supporting the collaboration. We thank C. Lange for XRD preparation, T. Wurst for his help in literature research, A. Schreiber for FIB preparation; image Fig. 2d was taken at ZELMI, TU Berlin, by U. Gernert. Thoughtful reviews by R. Gaupp and L.N. Warr helped to improve the manuscript, as well as the editorial comments by L. Williams.

REFERENCES

Armstrong, J.T. (1995) CITZAF: a package of correction programs for the quantitative electron microbeam X-ray-analysis of thick polished materials, thin films, and particles. Microbeam Analysis, 4, 177–200.

Banerjee, D.M. (1986) Proterozoic and Cambrian phosphorites - regional review: Indian subcontinent, *In:* P.J. Cook and J.H. Shergold (Eds), Phosphate deposits of the world Vol.1, Cambridge University Press, 70-87.

Banerjee, D.M., Schidlowski, M., and Arneth, J.D. (1986) Genesis of Upper Proterozoic-Cambrian phosphorite deposits of India: Isotopic inferences from carbonate fluorapatit, carbonate and organic carbon. Precambrian Research, 33, 239-253.

672 Banerjee, D.M., Deb, M., and Strauss, H. (1992) Organic carbon isotopic composition
673 of Proterozoic Sedimentary rocks from India: Preliminary Results: *In:* Schidlowski
674 et al. (Eds) Early Organic Evolution, Implications for Mineral and Energy
675 Resources, Springer Verlag, Heidelberg, 232-240.
676 Banerjee, D.M., Schidlowski, M., Siebert, F., and Brasier, M.D., (1997) Geochemical
677 changes across the Proterozoic-Cambrian transition in the Durmala phosphorite
678 mine section, Mussoorie Hills, Garhwal Himalaya, India. Paleogeography
679 Plaeoclimatology Paleoecology, 132, 183-194.
680 Battaglia, S. (2004) Variations in the chemical composition of illite from five
681 geothermal fields: a possible geothermometer. Clay Minerals, 39, 501-510.
682 Behar, F., Beaumont, V., De, B.P.H.L. (2001) Rock-Eval 6 technology: Performances
683 and developments. Oil and Gas Science and Technology 56, 111-134.
684 Bodine, M.W. and Loehr, C.A. (1979) Contact metamorphism of salt clays, Kerr-Mc-
685 Gee potash mine, Eddy County, New Mexico (abstract). 28th Annual Clay Mineral
686 Conference, Macon, Georgia, p 40.
687 Bourdelle, F., Parra, T., Beyssac, O., Chopin, C., and Vidal, O. (2013) Clay minerals
688 as geo-thermometer: A comparative study based on high spatial resolution analyses
689 of illite and chlorite in Gulf Coast sandstones (Texas, U.S.A.). American
690 Mineralogist, 98, 914-926.
691 Brasier, M.P. and Singh, P. (1987) Microfossils and Precambrian-Cambrian boundary
692 stratigraphy in Maldeota, Lesser Himalay, Geological Magazine, 124, 323-345.
693 Brindley, G.W., Zalba, P.E., and Bethke, C.M. (1983) Hydrobiotite, a regular 1:1
694 interstratification of biotite and vermiculite layers. American Mineralogist, 68,
695 420-425.
696 Burkins, D.L., Blum, J.D., Brown, K., Reynolds, R.C., and Erel, Y. (1999) Chemistry

and mineralogy of granitic, glacial soil chronosequence, Sierra Nevada Mountains, California. Chemical Geology, 162, 1-14.

Clarke, F. W. (1895) The constitution of the silicates. U.S. Geological Survey Bulletin, 125, pp 109.

Clauer, N. (2011) Another insight into illitization by K-Ar dating of micro- to nano-metric illite-type particles exchanged with alkylammonium cations. Clay Minerals, 46, 593-612.

Deocampo, D.M., Cuadros, J., Wing-Dudek, T., Olives, J., and Amouric, M. (2009) Saline lake diagenesis as revealed by coupled mineralogy and geochemistry of multiple ultrafine clay phases: Pliocene Olduvai Gorge, Tanzania. American Journal of Science, 309, 834-868.

Daniels, E.J., and Altaner, S.P. (1990) Clay mineral authigenesis in coal and shale from the Anthracite region, Pennsylvania. American Mineralogist, 75, 825-839.

Daniels, E.J., Aronson, J.L., Altaner, S.P., Clauer, N. (1994) Late Permian age of NH_4-bearing illite in anthracite from eastern Pennsylvania: Temporal limits on coalification in the central Appalachians. Geological Society of America Bulletin, 106, 760-766.

Dieckmann, V., Schenk, H.J., Horsfield, B., Welte, D.H. (1998) Kinetics of petroleum generation and cracking by programmed-temperature closed-system pyrolysis of Toarcian Shales. Fuel, 77, 23-31.

Ferry, J.M. (1976) Metamorphism of calcareous sediments in the Waterville-Vassalboro area, south-central Maine: Mineral reactions and graphical analysis. American Journal of Science, 276, 841-882.

Fleet, M.E. (2003) Sheet silicates: Micas. The Geological Society Publishing House, London, 2003, 2nd edition, 758 pp.

722 Fordham, A.W. (1990) Formation of trioctahedral illite from biotite in a soil profile
723 over granite gneiss. Clays and Clay Minerals, 38, 187-195.
724 Froehlich, P.N., Arthur, M.A., Burnett, W.C., Deakin, M., Hensley, V., Jahnke, R.,
725 Kaul, L., Kim, K.-H., Roe, K., Soutar, A., and Vathakanon, C. (1988) Early
726 diagenesis of organic matter in Peru continental margin sediments: Phosphorite
727 precipitation. In_ W.C. Burnett and P.N. Froehlich (Editors), The Origin of Marine
728 Phosphorite. The Results of the R.V. Robert D. Conrad Cruise 23-06 to the Peru
729 Shelf. Marine Geology, 80:309-343.
730 Guggenheim, S., Adams, J.M., Bain, D.C., Bergya, F., Brigatti, M.F., Drits, V.A.,
731 Formoso, M.L.L., Galán, E., Kogure, T., and Stanjek, H. (2006) Summary of
732 recommendations of nomenclature committees relevant to clay mineralogy: Report
733 of the Association Internationale pour l'Étude des Argilles (AIPEA) nomenclature
734 committes for 2006. Clays and Clay Minerals, 54, 761-772.
735 Gianfagna, A., Scordari, F., Mazziotti-Tagliani, S., Ventruti, G., and Ottolini, L.
736 (2007) Fluorophlogopite from Biancavilla (Mt. Etna, Sicily, Italy): Crystal
737 structure and crystal chemistry of a new F-dominant analog of phlogopite.
738 American Mineralogist, 92, 1601-1609.
739 Heimann, R.B. (2010) Classic and advanced ceramics - From fundamentals to
740 applications. Wiley-VCH Verlag GmbH & Co. KgaA, Weinheim, 553 pp.
741 Knudsen, A.C., and Gunter, M.E. (2002) Sedimentary phosphorites – an example:
742 Phosphoria Formation, Southeastern Idahoe, U.S.A. Reviews in Mineralogy and
743 Geochemistry, 48, 363-387.
744 Lee, J.H., Peacor, D.R., Lewis, D.D., and Wintsch, R.P. (1984) Chlorite-
745 illite/muscovite interlayered and interstratified crystals: A TEM/STEM study.
746 Contributions Mineralogy and Petrology, 88, 372-385.

747 Mazumdar, A. and Banerjee, D.M. (1998) Siliceous sponge spicules in the Early
748 Cambrian chert-phosphorite member of the Lower Tal Formation, Krol belt, Lesser
749 Himalaya. Geology, 26, 899–902.
750 Mazumdar, A. and Banerjee, D.M. (2001) Regional variations in the carbon isotopic
751 composition of phosphorite from the Early Cambrian Lower Tal Formation,
752 Mussoorie Hills, India. Chemical Geology, 175, 5-15.
753 Meunier, A. and Velde, B. (2004) Illite Origins, Evolution and Metamorphism.
754 Springer, Berlin, Heidelberg, New York, 2004, 286 pp.
755 Monier, G. and Robert, J.-L. (1986) Muscovite solid solutions in the system K_2O-
756 MgO-FeO-Al_2O_3-SiO_2-H_2O: an experimental study at 2 kbar P_{H2O} and comparison
757 with natural Li-free white micas. Mineralogical Magazine, 50, 257-266.
758 Moore, D.M. and Reynolds, R.C. (1989) X-ray diffraction and the identification and
759 analysis of clay minerals. Oxford University Press, Oxford New York, 1989, 332
760 pp.
761 Nettleton, W.D., Nelson, R.E., and Flach, K.W. (1973) Formation of mica in surface
762 horizons of dryland soils. Soil Science of America Proceedings, 37, 473-478.
763 Parnell, R.A., Jr. (1983) Weathering processes and pickeringite formation in a sulfidic
764 schist: A consideration in acid precipitation neutralization studies. Environmental
765 Geology, 4, 209-215.
766 Persson, L. and Pösson, S. (2000) Abiotic characteristics of soils suppressive to
767 Aphanomyces root rot. Soil Biology and Biochemistry, 32, 1141-1150.
768 Pyle, J.M., Spear, F.S, and Wark, D.A. (2002) Electron microprobe analysis of REE
769 in apatite, monazite and xenotime: Protocols and Pitfalls. Reviews in Mineralogy
770 and Geochemistry, 48, 337-362.
771 Rieder, M., Cavazzini, G., D'Yakonov, Y.S., Frank-Kamenetskii, V.A., Gottardi, G.,

Guggenheim, S., Koval, P.V., Müller, G., Neiva, A.M.R., Radoslovich, E.W., Robert, J.-L., Sassi, F.P., Takeda, H., Weiss, Z., and Wones, D. (1998) Nomenclature of the micas. Canadian Mineralogist, 36, 905-912.

Sato, T., Iwabuchi, Y., Iijima, A., Oinuma, K. and Kobayashi, K. (1965) Geological research on the bottom sediments sampled by the Fifth Japanese Antarctic Research Expedition Japanese Antarctic Research Expedition (1956-62), Science Report, Series C, 4, 42 pp.

Schenk, H.J., Di Primio, R., Horsfield, B. (1997) The conversion of oil into gas in petroleum reservoirs. Part 1: Comparative kinetic investigation of gas generation from crude oils of lacustrine, marine and fluviodeltaic origin by programmed-temperature closed-system pyrolysis. Organic Geochemistry 26, 467-481.

Schlager, W. (2005) Carbonate sedimentology and sequence stratigraphy. Society for Sedimentary Geology, Tulsa, Oklahoma, USA, 200 pp.

Scordari, F., Schingaro, E., Ventruti, G., Nicotra, E., Viccaro, M., and Tagliani, S.M. (2013) Fluorophlogopite from Piano delle Concazze (Mt. Etna, Italy): Crystal chemistry and implications for the crystallization conditions. American Mineralogist, 98, 1017-1025.

Shell, H.R., and Ivey, K.H. (1969) Fluorine micas. Unites States Bureau of Mines Bulletin, 647.

Singh, S.K., Trivedi J.R., Pande, K., Ramesh, R., and Krishnaswami, S. (1999) Re-Os isotope systematics in black shales from the Lesser Himalaya: Their chronology and role in the $^{187}Os/^{188}Os$ evolution of seawater. Geochimica et Cosmochimica Acta, 63, 2381–2392.

Soveri, U. (1956) The mineralogical composition of argillaceous sediments of Finland. Annales Academie Sciences Fennlandia, 48, Ser. AIII, 32 pp.

797 Spear, F.S. (1993) Metamorphic phase equilibria and pressure-temperature-time paths.
798 Mineralogical Society of America Monograph Series, Washington 1993, 799 pp.
799 Srodón, J. and Eberl, D.D. (1984) Illite. Reviews in Mineralogy, 13, 495-544.
800 Strunz, H. and Nickel, E. H. (2001) Strunz Mineralogical Tables. Chemical-structural
801 mineral classification system. E. Schweitzerbart'sche Verlagsbuchhandlung
802 (Nägele u. Obermiller), Stuttgart 2001, 870 pp.
803 Weiss, A., Scholz, A. and Hofmann, U. (1956) Zur Kenntnis von trioktaedrischem
804 Illit. Zeitschrift für Naturforschung, 11b, 429-430.
805 Trappe, J. (1993) Phanerozoic phosphorite depositional systems. Springer, Berlin,
806 Heidelberg, New York, 1993, 316 pp.
807 Ushizawa, N. (1981) Trioctahedral ilites from two talc mines in southwestern
808 Hokkaido. Clay Science, 5, 299-304.
809 Walker, G.F. (1950) Trioctahedral minerals in the soil-clays of north-east Scotland.
810 Mineralogical Magazine, 29, 72-84.
811 Weiss, H.M., Wilhelms, A., Mills, N., Scotchmer, J., Hall, P.B., Lind, K. and Brekke,
812 T. (2000): NIGOGA - The Norwegian Industry Guide to Organic Geochemical
813 Analyses [online]. Edition 4.0 Published by Norsk Hydro, Statoil, Geolab Nor,
814 SINTEF Petroleum Research and the Norwegian Petroleum Directorate. 102 pp
815 [cited 2014-02-05]. Available from World Wide Web:
816 <http://www.npd.no/engelsk/nigoga/default.htm>.
817 Wilson, M. J. (1967) The clay mineralogy of some soils derived from a biotite-rich
818 quartz-gabbro in the Strathdon area, Aberdeenshire. Clay Minerals, 7, 91.
819 Wirth, R. (2004) Focused Ion Beam (FIB): A novel technology for advanced
820 application of micro- and nanoanalysis in geosciences and applied mineralogy.
821 European Journal of Mineralogy, 16, 863-877.

Wirth, R., (2009) Focused Ion Beam (FIB) combined with SEM and TEM: Advanced analytical tools for studies of chemical composition, microstructure and crystal structure in geomaterials on a nanometre scale. Chemical Geology, 261, 3-4, 217-229.

Zhu, C. and Sverjensky, D.A. (1992) F-Cl-OH partitioning between biotite and apatite. Geochimica Cosmochimica Acta, 56, 3435-3467.

FIGURE CAPTIONS

Figure 1. a) Scanned image of cut and polished surface of phosphatic mudstone with alternating layers of sparitic dolostone (handspecimen DUR-7 from Durmala section, Krol Formation, India); rectangle shows approximate position of thin section (b), taken from the opposite part of the rock slice. The mudstone layers are partly brecciated, and sparitic irregular dolomite veins crosscut the layers. b) Scanned image of thin section; white rectangle shows position of Fig. 2a, black rectangle position of Fig. 2d. The finely laminated mudstone layers consist dominantly of extremely fine-grained apatite with a high amount of organic matter, the sparitic layers of coarse grained dolomite.

Figure 2. BSE images of dolostone and apatite-rich layers; a) overview of the occurrence of fluorophlogopite with coarse-grained dolomite in organic matter (C_{org}), which fills interstices between dolomite; inset shows detail in b). The position for the TEM foil cut by focused ion beam (see Fig. 5a) is indicated. Dolomite is slightly zoned with Ca-rich inner parts. Calcite formed along cracks and on boundaries to organic matter; white rectangle shows position of c), enlarged image of aggregates of fluorophlogopite; inset shows detail in c), showing the subparallel orientation of the crystals; organic matter is also included parallel to the layers, and the bright contrasting nm-sized crystals are apatite. d) Laminated mudstone layer; bedding is horizontal. Organic matter is concentrated in ovoid and elongated structures within fine-grained apatite. Dolomite is present in round structures, (most) likely mimicking former sedimentary or organic structures. Irregular grain boundaries of quartz or quartz+mica aggregates point to silification, not to detrital quartz. Pyrite is present as

854 euhedral crystals, tens of µm large, but is additionally present as framboid crystals
855 together with rare sphalerite (see Appendix Fig. 1); rectangle labeled 013 shows
856 position of e), showing a vesicle filled with organic matter and mica. Note the
857 botryoidal shape of apatite; dark within this apatite (type I) are inclusions of C_{org} and
858 small pores. Mica forms irregular aggregates, particles are << 1 µm thick and only a
859 few µm long, concentrated at the rim of the ovoid structure and oriented with the
860 elongation approximately perpendicular to the rim. The position for the TEM foil cut
861 by focused ion beam (see Fig. 6) is indicated. f) Enlarged part of a vesicle filled with
862 organic matter and mica; note the extremely fine-grained mica layer packages.
863
864 Figure 3. BSE images of fluorophlogopite in the phosphatic mudstone layer; a) shows
865 to the left fluorophlogopite overgrowing illite, to the right a vesicle filled with organic
866 matter, calcite and fluorophlogopite. b) is enlarged area of a) with different contrast to
867 highlight the conspicuous grain boundary towards organic matter. In contrast to
868 examples shown in Fig. 2, boundaries are straight and curved and indicate former
869 unidentifiable structures in the organic matter. Scale bar at bottom is ~10 µm.
870
871 Figure 4. BSE images (a,b) and X-ray mapping (c-f), showing fluorophlogopite in the
872 textural position surrounding illite. a) fluorophlogopite is surrounded by apatite (two
873 types, apatite I is botryoidal with high porosity and C_{org} inclusions, apatite II is clear
874 and hypidiomorphic to idiomorphic) and overgrows illite. Illite has a round inner part
875 and a rim, enriched in V. b) Detail of the right part of a), with different contrast to
876 highlight the transition from illite in the center to V-illite and fluorophlogopite. c) X-
877 ray map for F indicates enrichment in the V-illite and strong enrichment in
878 fluorophlogopite. Apatite I and II are both F-apatite. d) X-ray map for V shows strong

879 enrichment (up to 5 wt% V_2O_3) in the tip of the small outgrowing crystals. e) and f)
880 compare the Mg and Al contents of illite, V-illite and fluorophlogopite.
881 fluorophlogopite and illite are clearly separated from each other and there are no
882 indications for small-scale mixtures.
883
884 Figure 5. BSE images of illite with overgrowths of fluorophlogopite (a, b,d) and X-
885 ray mapping (c,e-g); a) tip of illite with overgrowth of fluorophlogopite next to
886 dolomite. The white layer in illite is apatite. b) Same area after repolishing, i.e.
887 several µm deeper in thin section; the ellipsoidal dolomite grain has inclusions of
888 fragmented botryoidal apatite I, the extensional crack (compare a) crosscuts illite,
889 dolomite as well as apatite I in the dolomite. The extensional crack (enlarged BSE
890 image in (d) highlighted by circles) within the mica is offset into several parts parallel
891 to (001). X-ray mapping confirms F-apatite and the fluorophlogopite (c,e),
892 overgrowing especially the tip of the illite crystal. K-mapping (f) indicates that the
893 mineral within the extensional crack (compare with Fig. d) is not mica, but due to its
894 sheet mineral appearance probably chlorite. Ca-mapping (g) confirms apatite in layers
895 parallel to (001) of the mica.
896
897 Figure 6. Chemical composition of micas from sample DUR7 (WDS electron
898 microprobe data), in terms of atoms per formula unit (pfu), calculated on the basis of
899 22 oxygen. a) The sum of octahedral cations vs. the sum of the interlayer (dominantly
900 K, with minor amounts of NH_4 in fluorophlogopite = F-phlog; white diamond is
901 average of all analyses); both mica types are clearly interlayer deficient, and both
902 show a slight solid solution component between tri- and dioctahedral. One analysis of
903 V-illite with sum oct 4.5 from the V-rich tip of the crystal is influenced by

904 overlapping of the beam with the surrounding fluorophlogopite. Open square
905 indicates average composition including V-rich analyses. b) Si contents are more
906 variable in illite compared to fluorophlogopite, and the V-illite has the highest Si
907 content. c) Mg vs. Fe contents show that illite is quite variable in both Mg and Fe, V-
908 illite and fluorophlogopite have only small Fe-contents. d) The V-rich rim of illite
909 shows a clear tendency for a substitution V = Al; fluorophlogopite is low in V. e) The
910 three types of mica are also clearly distinguished by their F-contents; fluorophlogopite
911 has > 50 mol% of the F-endmember.
912
913 Figure 7. TEM images of fluorophlogopite (Mg-mica) within the sparitic dolostone
914 layer (cf. Fig. 2d); a) HAADF image of FIB-cut foil (# 3234). Circles (1, 2) indicate
915 areas for EELS analysis, rectangle (BF 01) is position of b). Round structures in the
916 background result from the TEM grid. The bright spot in the lower left is a cavity
917 filled with Pt and Ga from the FIB cutting procedure. b) Bright-field image of
918 fluorophlogopite and organic matter (C org). White areas in mica are void (cleavage-
919 parallel porosity). The phase boundary is also characterized by a low contrast and
920 void areas in the upper part. Rectangular dark areas in upper part of the image result
921 from beam damage during energy dispersive analysis. c) Bright-field image of phase
922 boundary between organic matter and fluorophlogopite. The phase boundary is
923 approximately 30 nm wide. Different grey-black contrasting areas in mica indicate
924 slightly different orientation of the layer packages. d) High-resolution image of
925 fluorophlogopite; inset shows selected area diffraction pattern. Individual layer
926 packages are 7 to 13 layers thick, separated by a low-angle grain boundary and each
927 layer is 10.1 Å thick. Arrows indicate stacking faults. e) High-resolution image of the
928 interface mica–organic matter; inset shows selected area diffraction pattern of organic

matter of the upper part of the image. Over a width of ~20 nm (indicated by lines), it shows no structure. Further away, a slight structure is visible in the HRTEM image, verified by rings in the SAD pattern.

Figure 8. HAADF (a,b) and darkfield (c) images of fluorophlogopite-illite intergrowths in a vesicle filled with organic matter (C org) at the border to apatite, from the phosphatic mudstone layer (see Fig. 2e). Mica layer packages are irregularly oriented and vary in length and width strongly. At the transition between apatite and organic matter, a porous zone (por) is marked in (b). d) enlarged part of the border between apatite and organic matter, position slightly below area shown in (b) and the corresponding EDS spectrum of fluorophlogopite; Ga and Cu peaks result from the Ga-ion cutting procedure and underlying Cu grid, respectively. e,f) show enlarge parts of b with position of the EDS analysis. Illite and fluorophlogopite are distinguished by their Al/Mg.

Figure 9. Electron energy-loss spectra of fluorophlogopite from the dolostone layer; (a) shows the deconvoluted spectrum with the labeled peaks for C (inclusions within the mica), K and N, (b) the original spectrum, (c) the deconvoluted spectrum for F.

FIGURES FOR APPENDIX

Figure 1 Appendix. BSE images of sample DUR-7, showing pyrite in large crystals (upper image, left; recrystallized pyrite II) together with pyrite framboids (middle and lower images). Middle image shows same area as upper image, but with different contrast, to highlight sphalerite, which rarely occurs; lower image is enlarged part of the central area.

954

955 Figure 2 Appendix. X-ray powder diffraction pattern of fraction <2 μm, separated
956 from sample DUR-7; upper part shows textured preparation at air dried conditions,
957 glycolated and heated to 550°C. Lower part shows the area of the (060)-peaks for
958 dioctahedral-trioctahedral layer silicates; Mg-mica = fluorophlogopite.

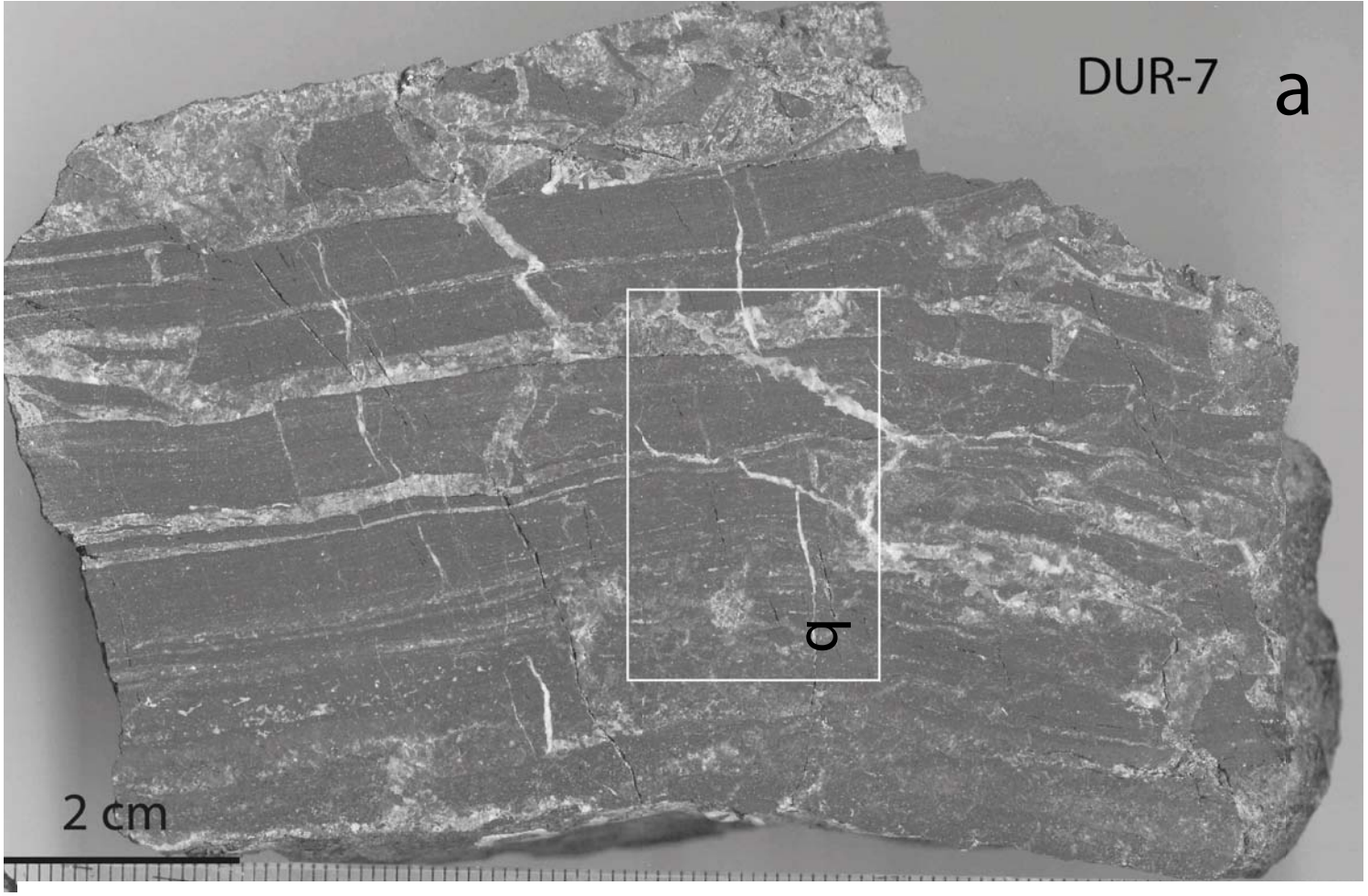
DUR-7
a
b
2 cm

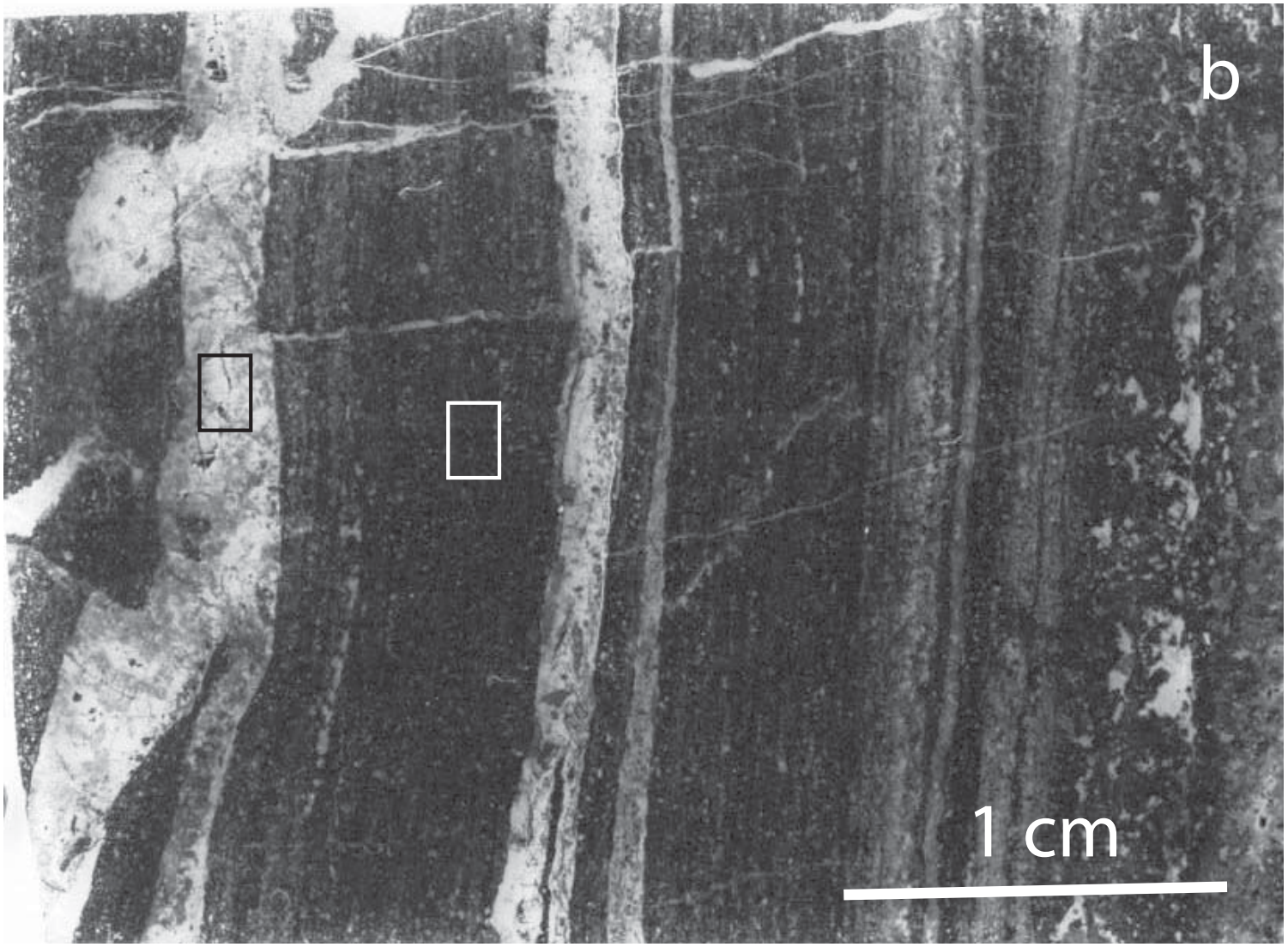
b
1 cm

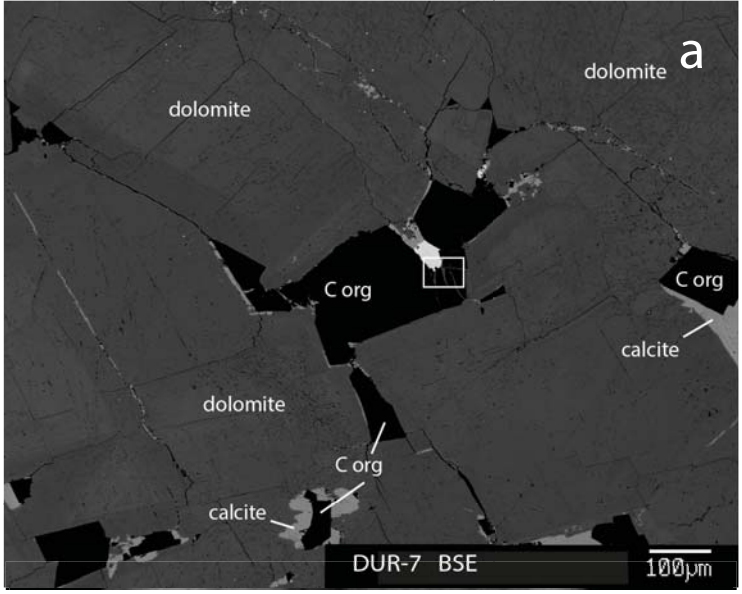
a
dolomite
dolomite
C org
C org
calcite
dolomite
C org
calcite
DUR-7 BSE
100µm

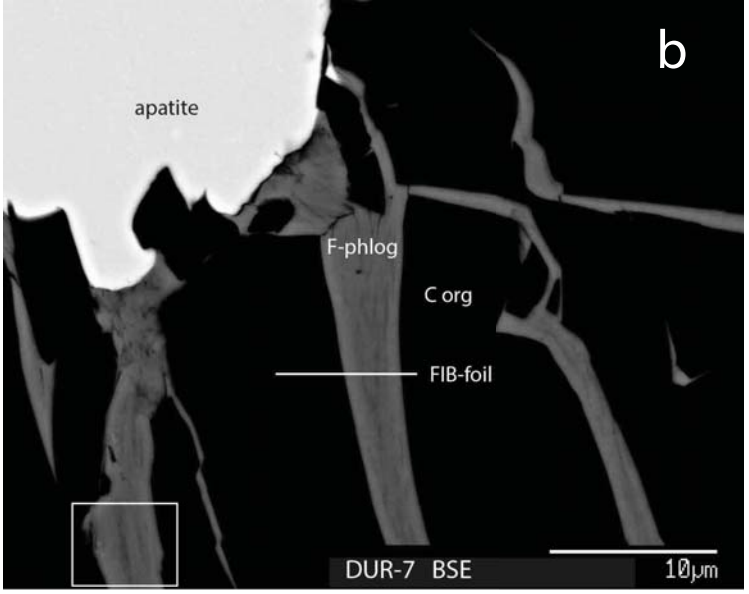
b
apatite
F-phlog
C org
FIB-foil
DUR-7 BSE
10µm

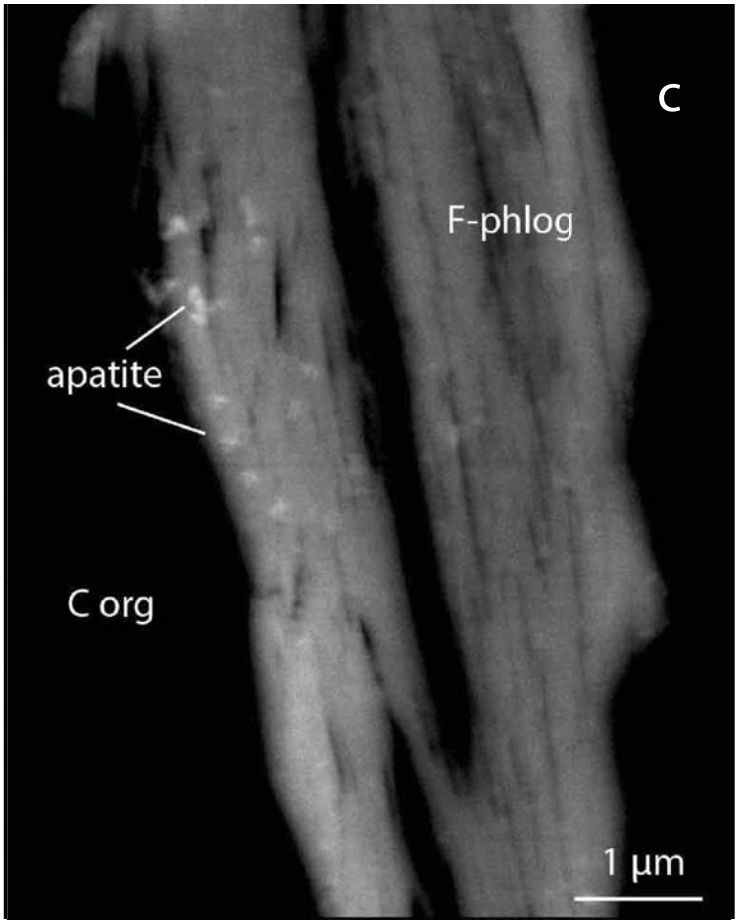
c
F-phlog
apatite
C org
1 µm

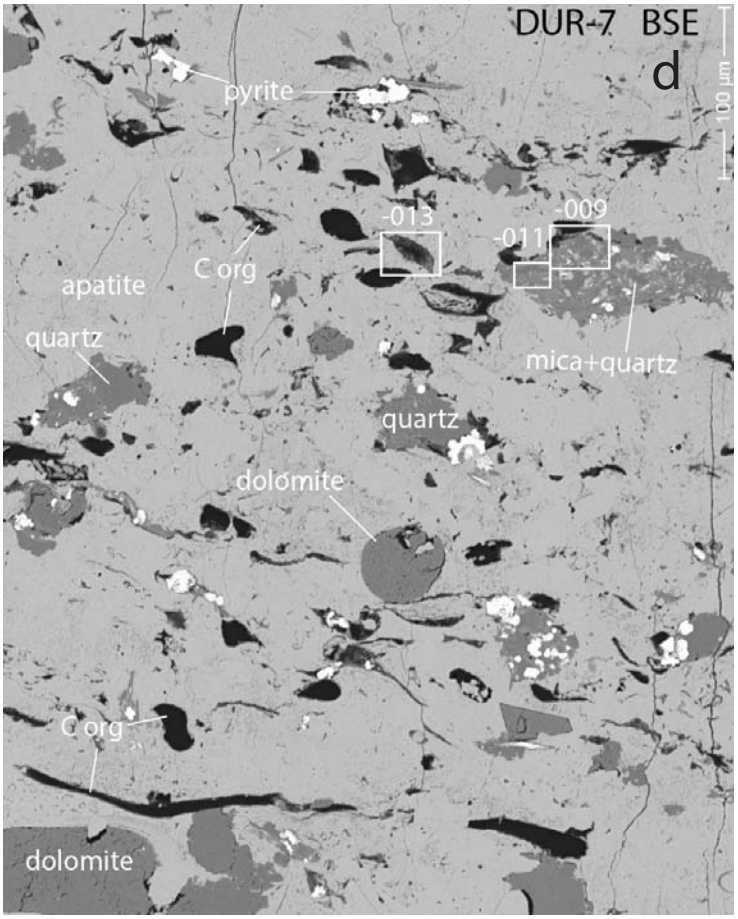
DUR-7 BSE
d
pyrite
-013
-009
-011
C org
apatite
quartz
mica+quartz
quartz
dolomite
C org
dolomite

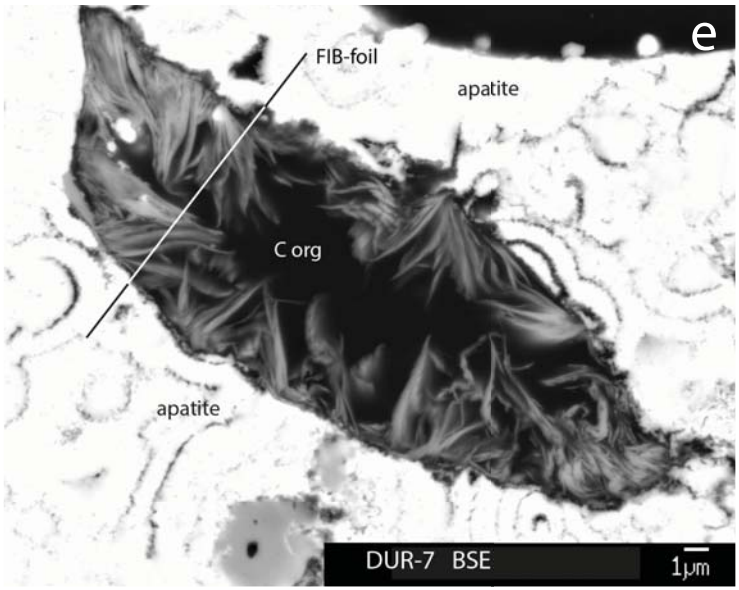
e
FIB-foil
apatite
C org
apatite
DUR-7 BSE
1µm

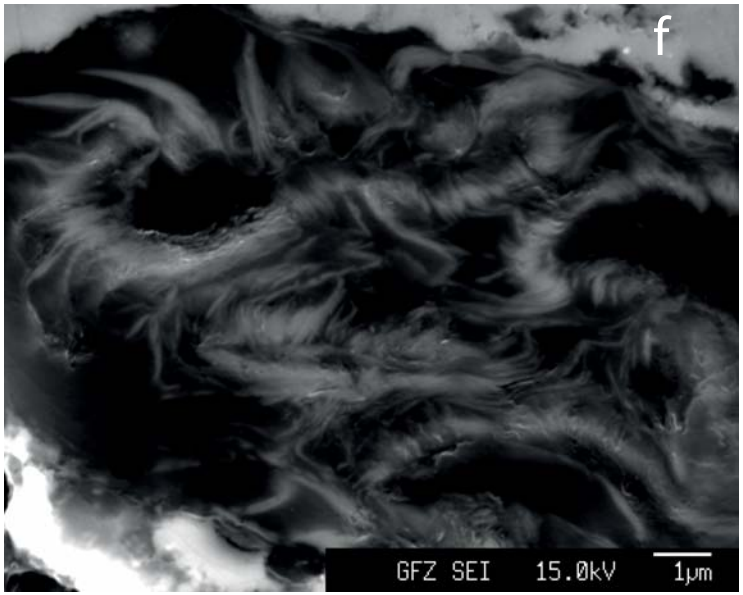
f
GFZ SEI 15.0kV
1µm

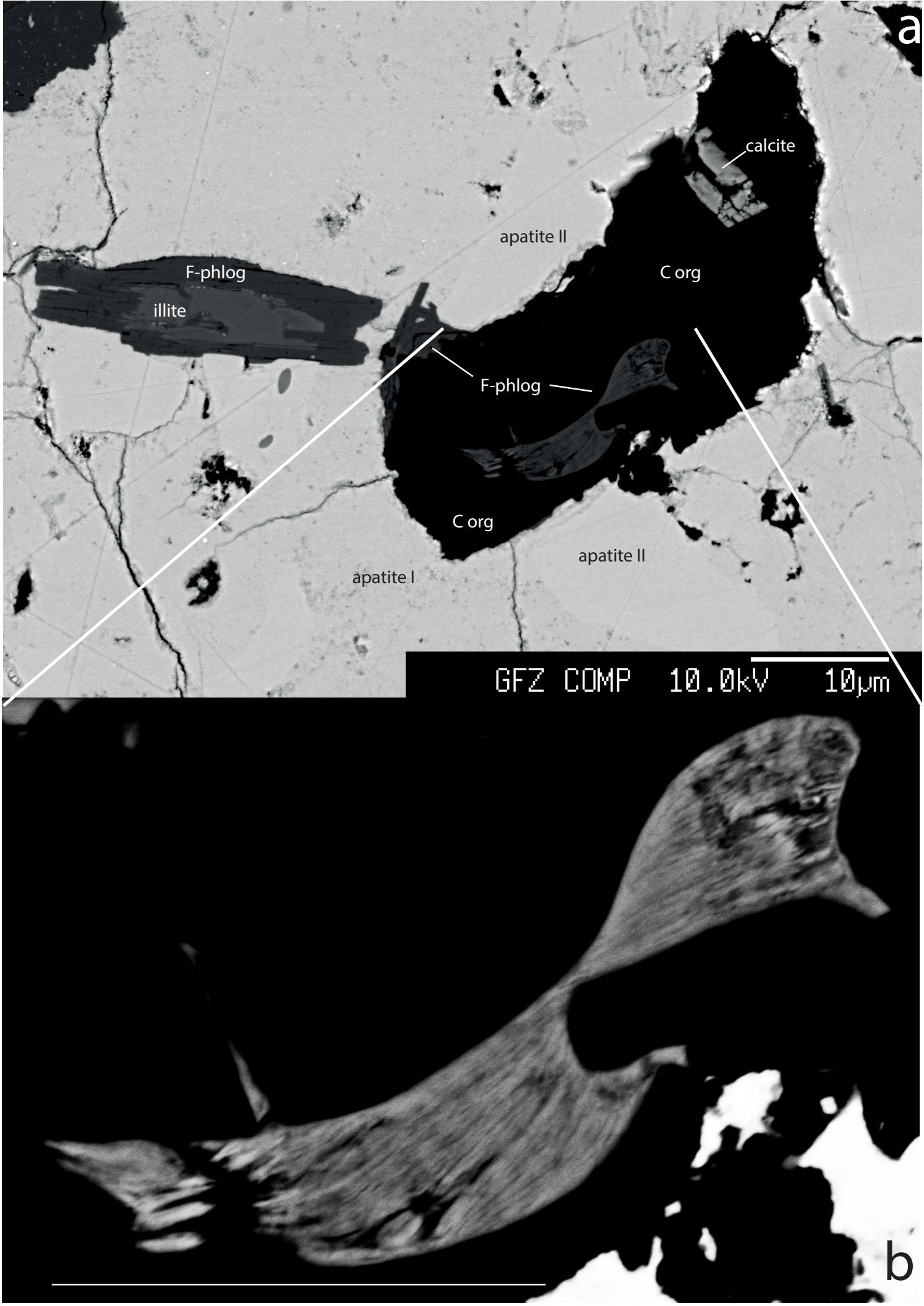
a
calcite
apatite II
F-phlog
illite
C org
F-phlog
C org
apatite II
apatite I
GFZ COMP 10.0kV 10µm
b

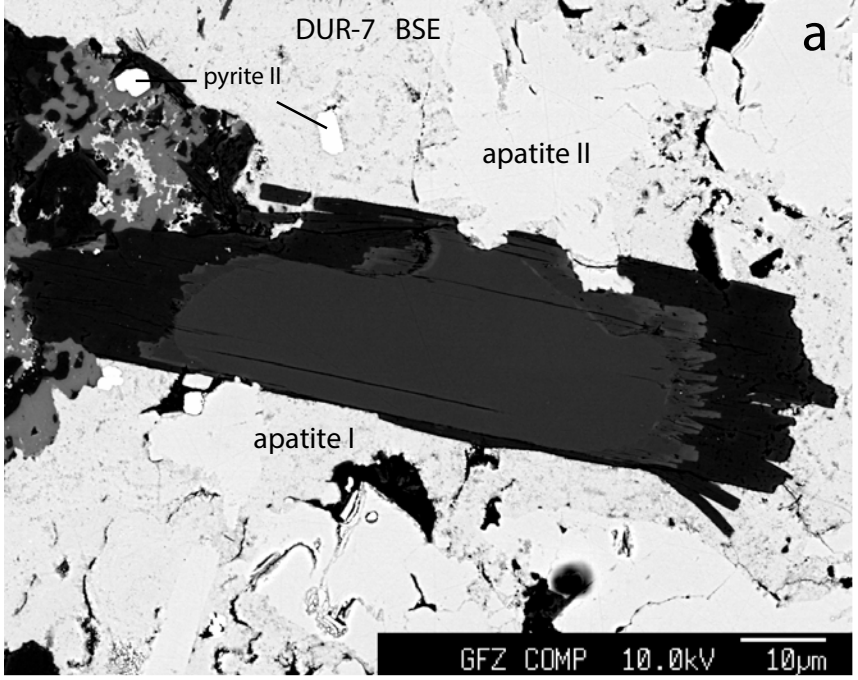
DUR-7 BSE
a
pyrite II
apatite II
apatite I
GFZ COMP 10.0kV 10µm

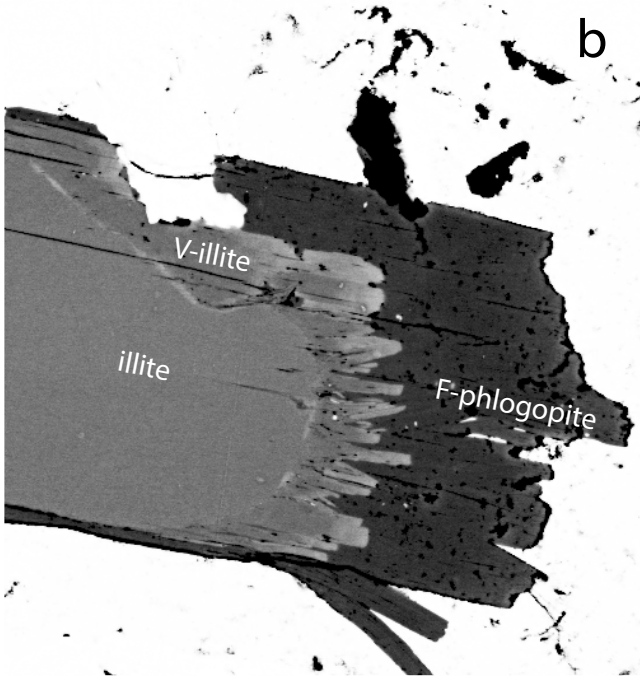
b
V-illite
illite
F-phlogopite

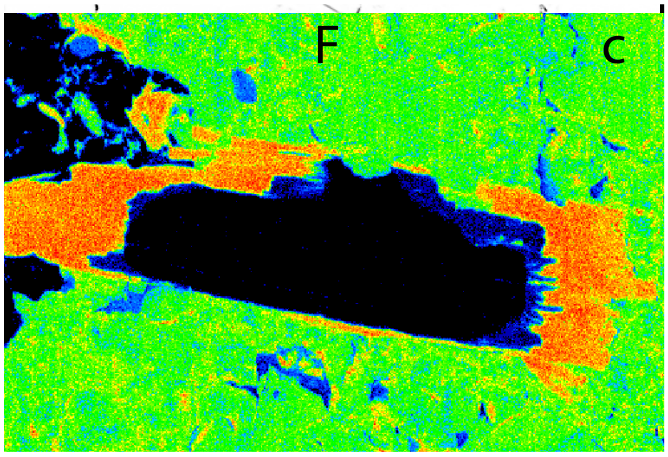
F
c

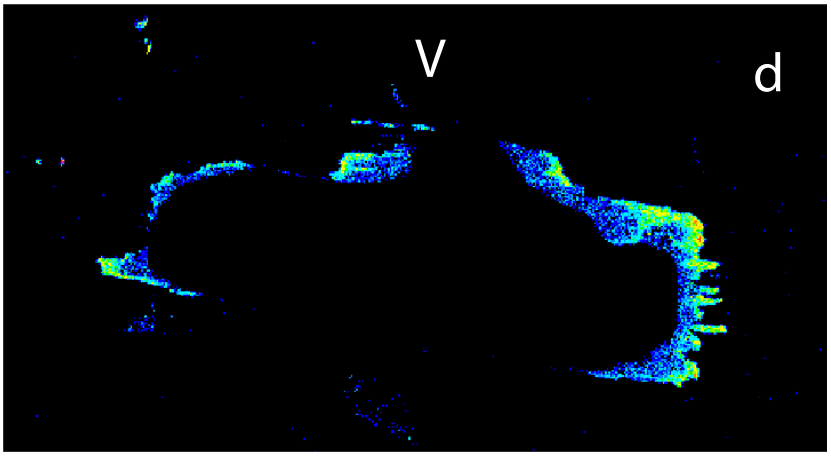
V
d

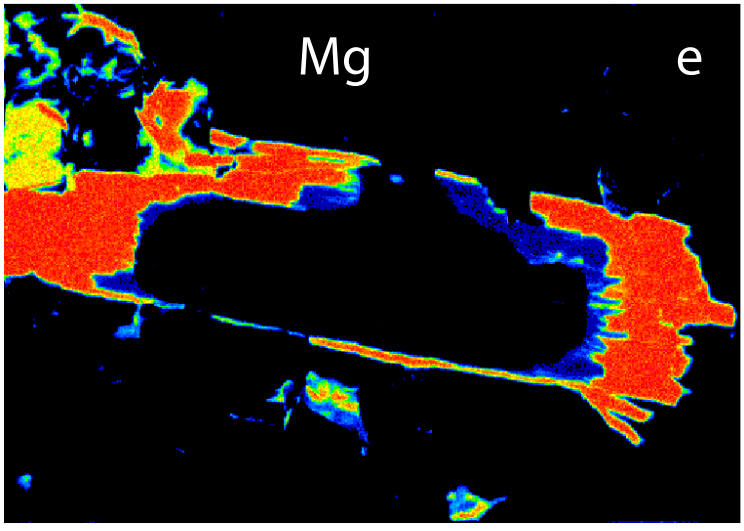
Mg
e

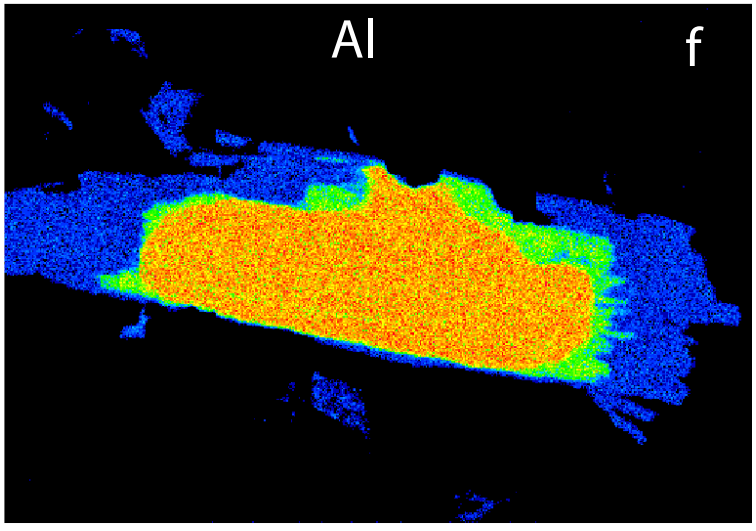
Al
f

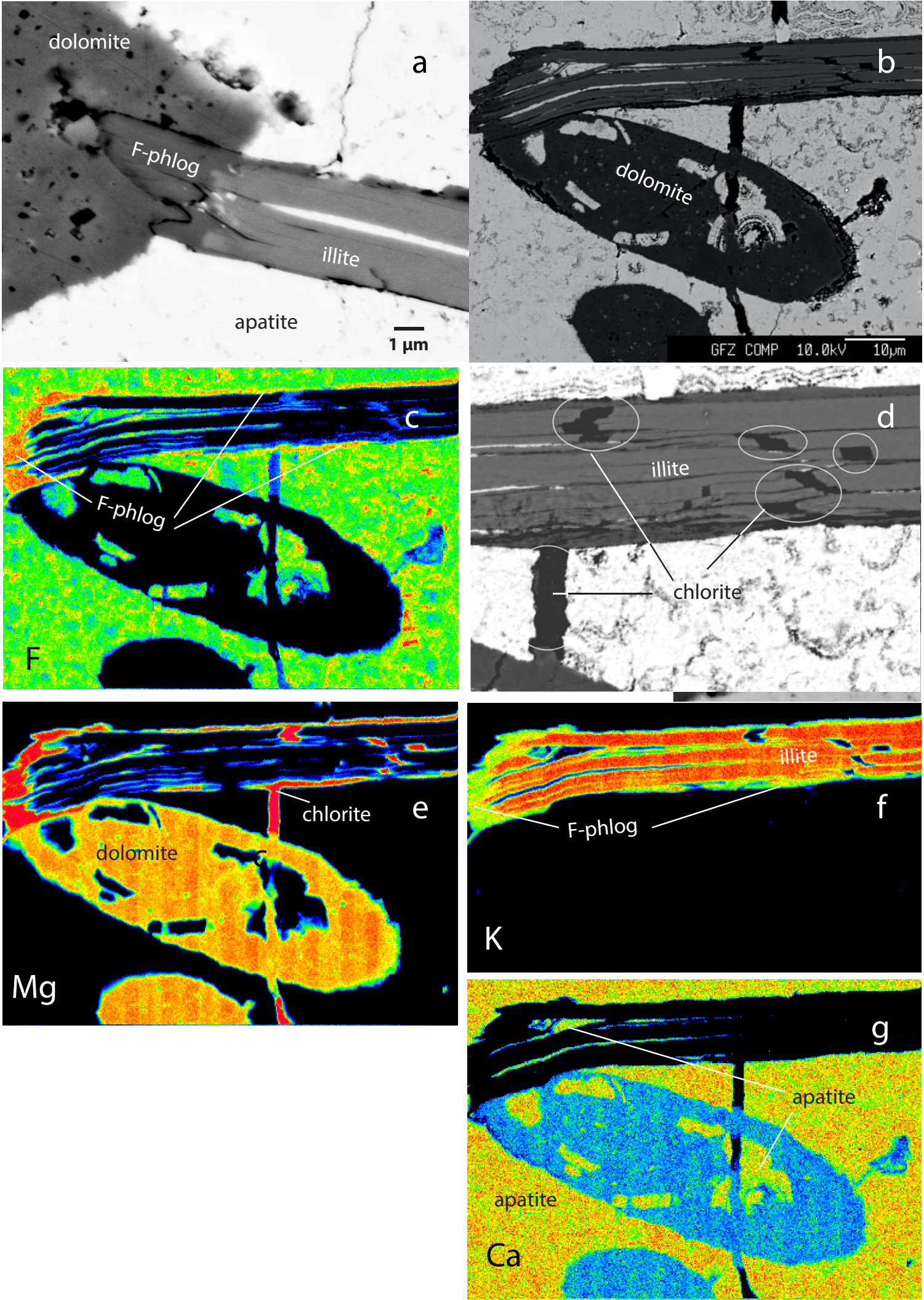
dolomite
a
F-phlog
illite
apatite
1 µm
b
dolomite
GFZ COMP 10.0kV 10µm
c
F-phlog
F
d
illite
chlorite
e
chlorite
dolomite
Mg
f
illite
F-phlog
K
g
apatite
apatite
Ca

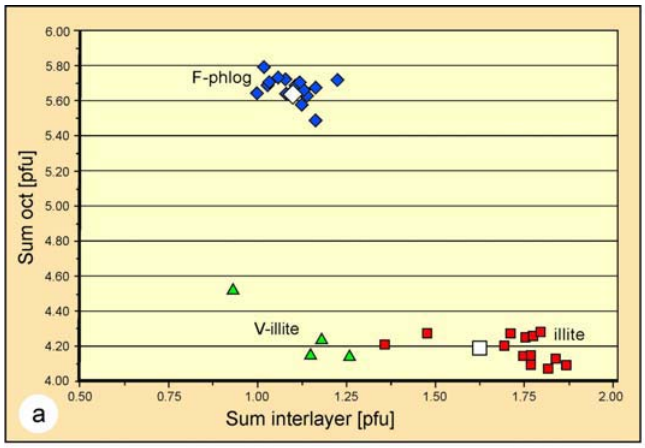
F-phlog
V-illite
illite
Sum oct [pfu]
Sum interlayer [pfu]
a

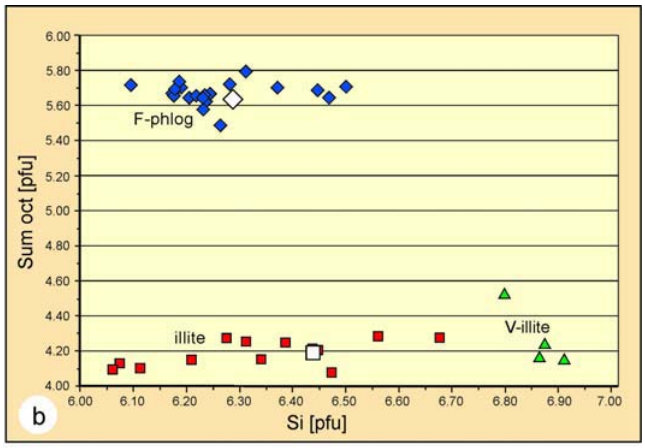
F-phlog
illite
V-illite
Sum oct [pfu]
Si [pfu]
b

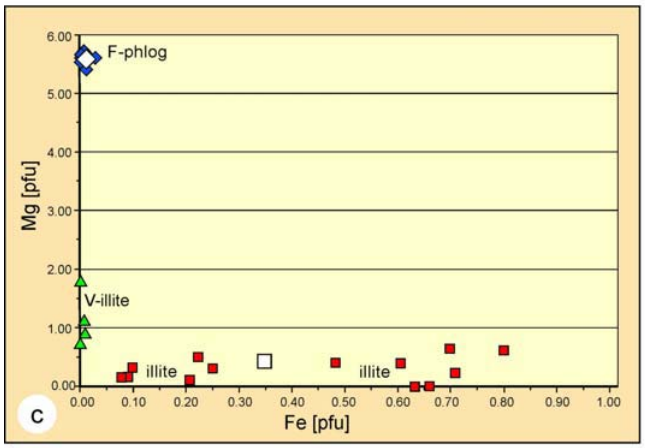
F-phlog
V-illite
illite
illite
Mg [pfu]
Fe [pfu]
c

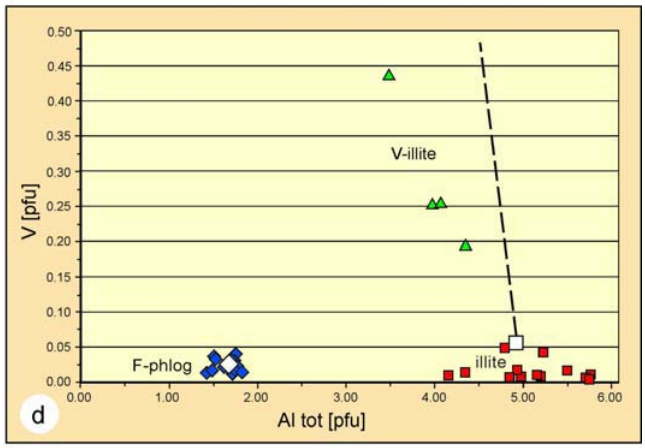
V-illite
F-phlog
illite
V [pfu]
Al tot [pfu]
d

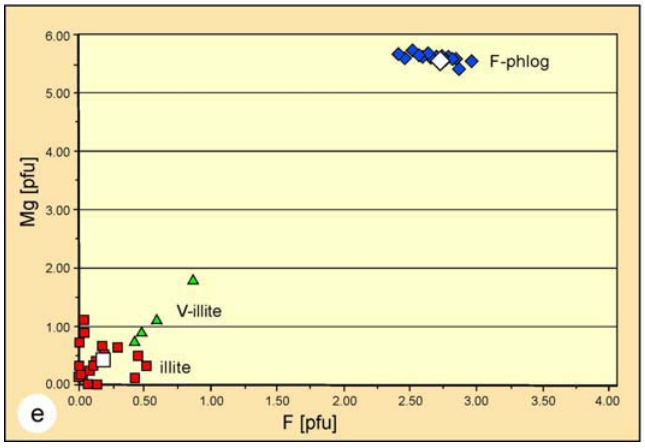
F-phlog
V-illite
illite
Mg [pfu]
F [pfu]
e

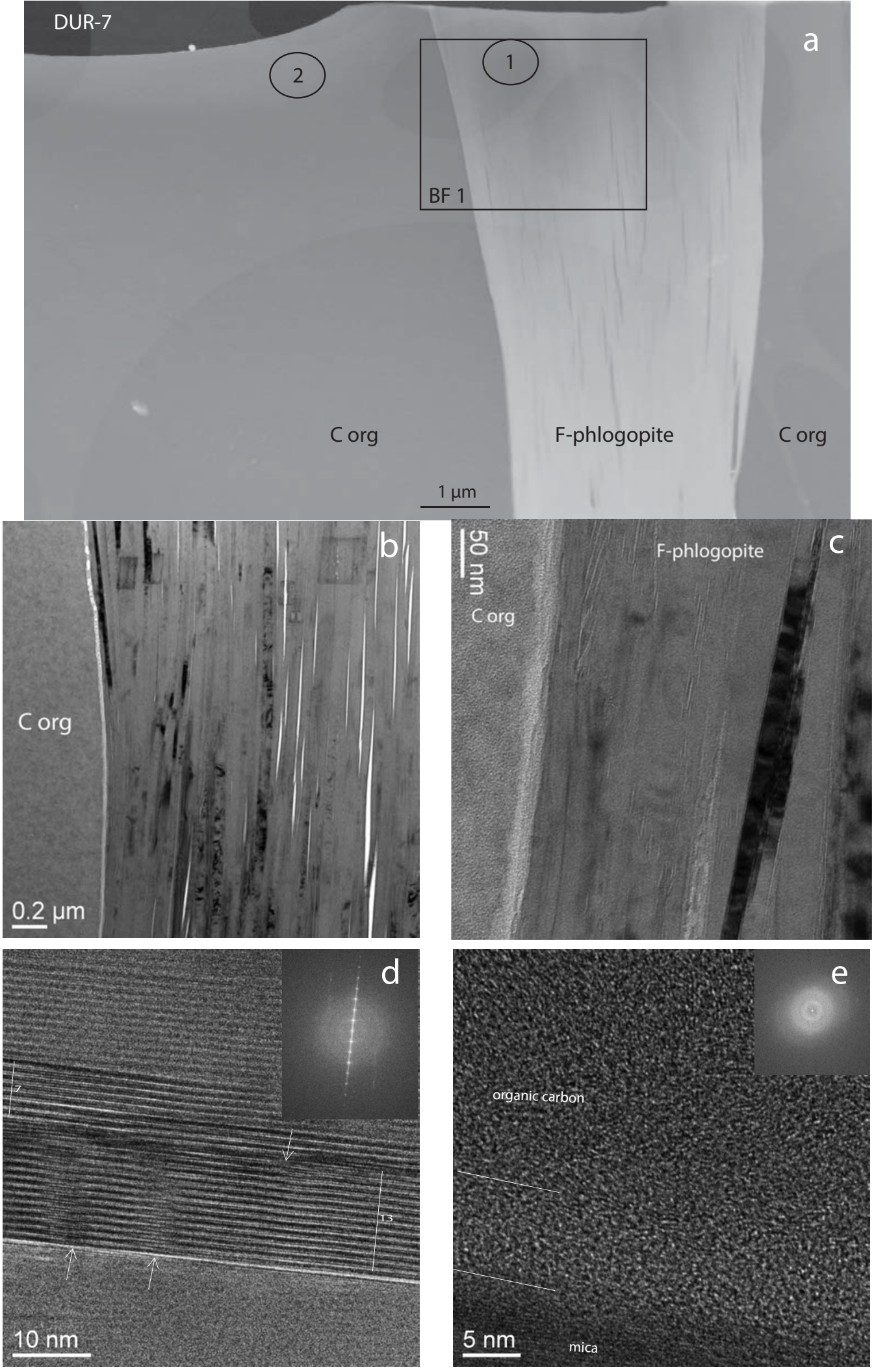
DUR-7
a
1
2
BF 1
C org
F-phlogopite
C org
1 µm
b
C org
0.2 µm
50 nm
F-phlogopite
c
C org
d
7
13
10 nm
e
organic carbon
5 nm
mica

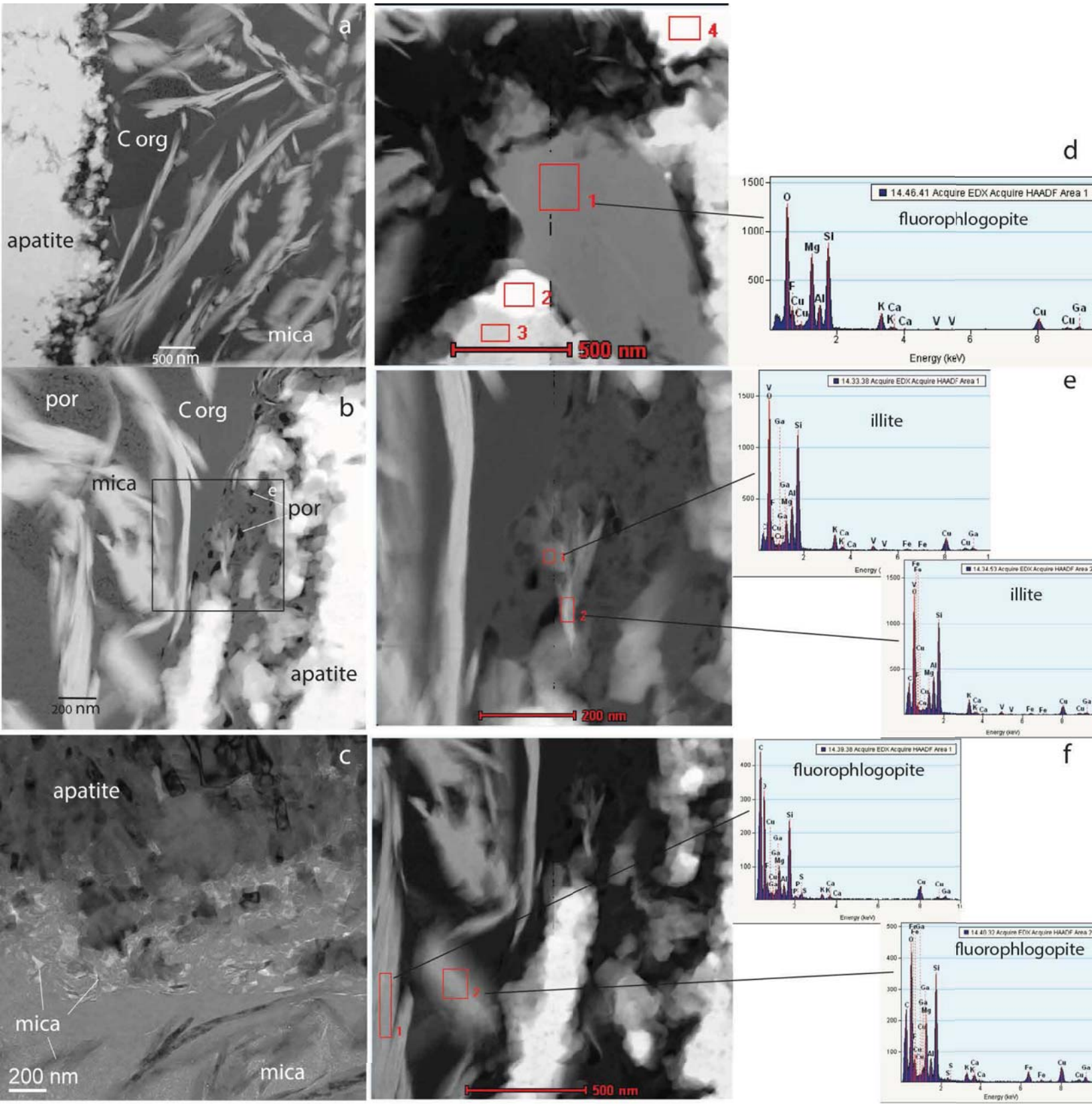
a
C org
apatite
mica
500 nm
4
1
2
3
500 nm
d
14.46.41 Acquire EDX Acquire HAADF Area 1
fluorophlogopite
Energy (keV)
por
C org
b
mica
e
por
apatite
200 nm
200 nm
e
14.33.38 Acquire EDX Acquire HAADF Area 1
illite
14.34.53 Acquire EDX Acquire HAADF Area 2
illite
c
apatite
mica
mica
200 nm
500 nm
f
14.39.38 Acquire EDX Acquire HAADF Area 1
fluorophlogopite
14.40.33 Acquire EDX Acquire HAADF Area 2
fluorophlogopite

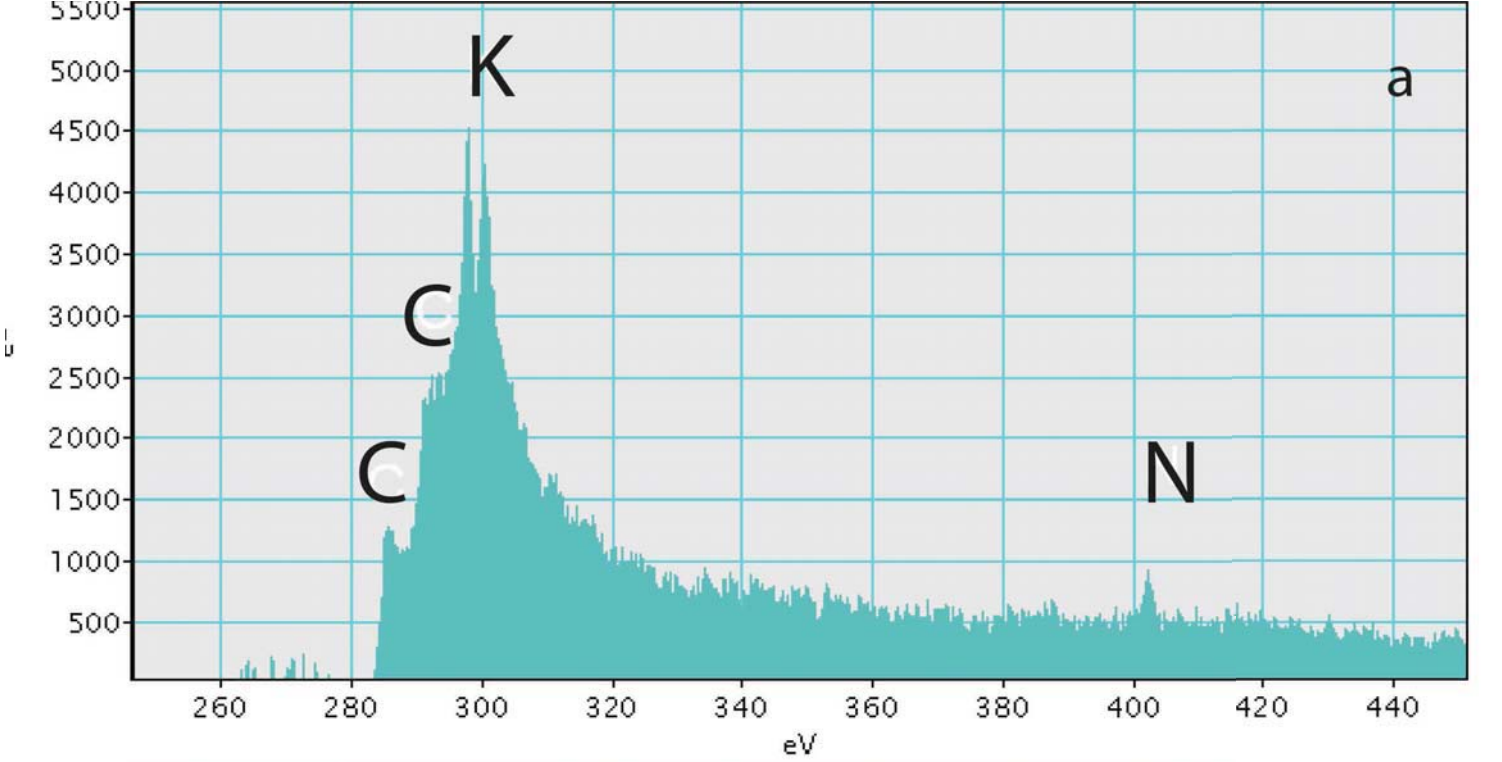
K
C
C
N
a
e-
eV

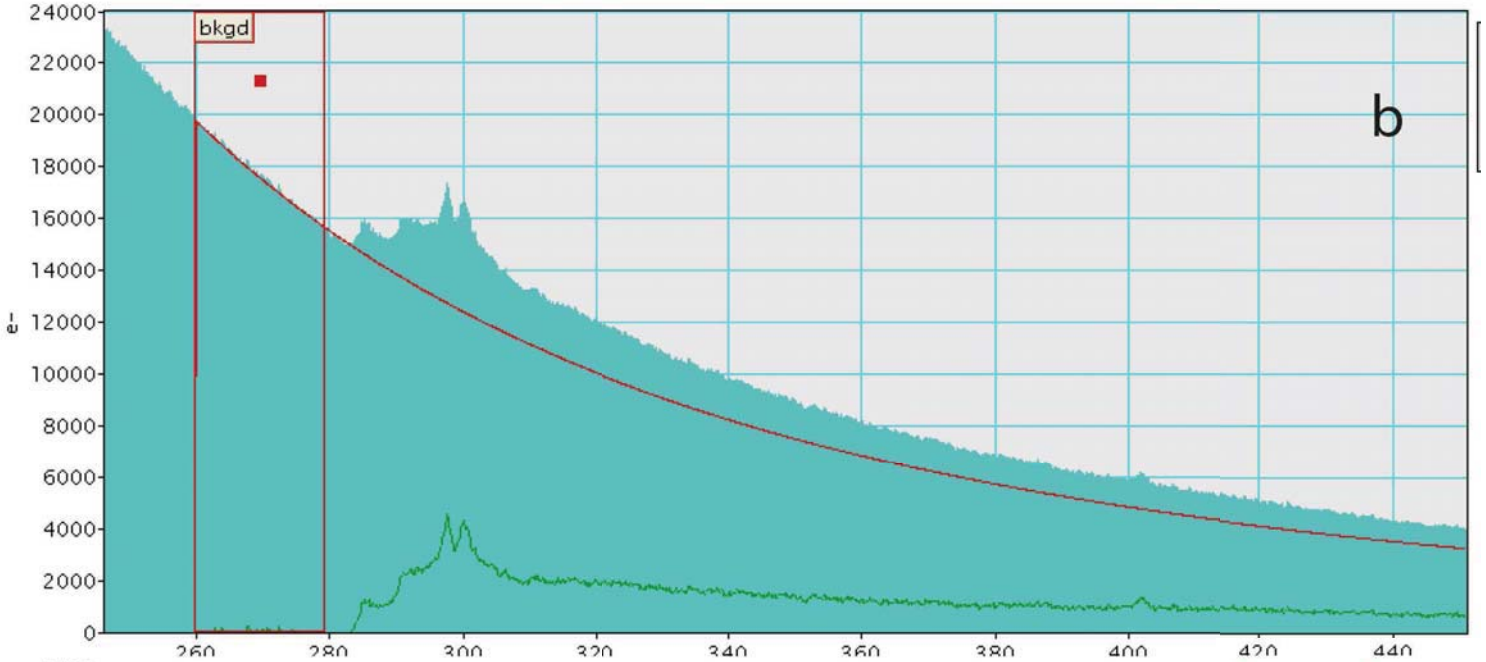
bkgd
b
e-

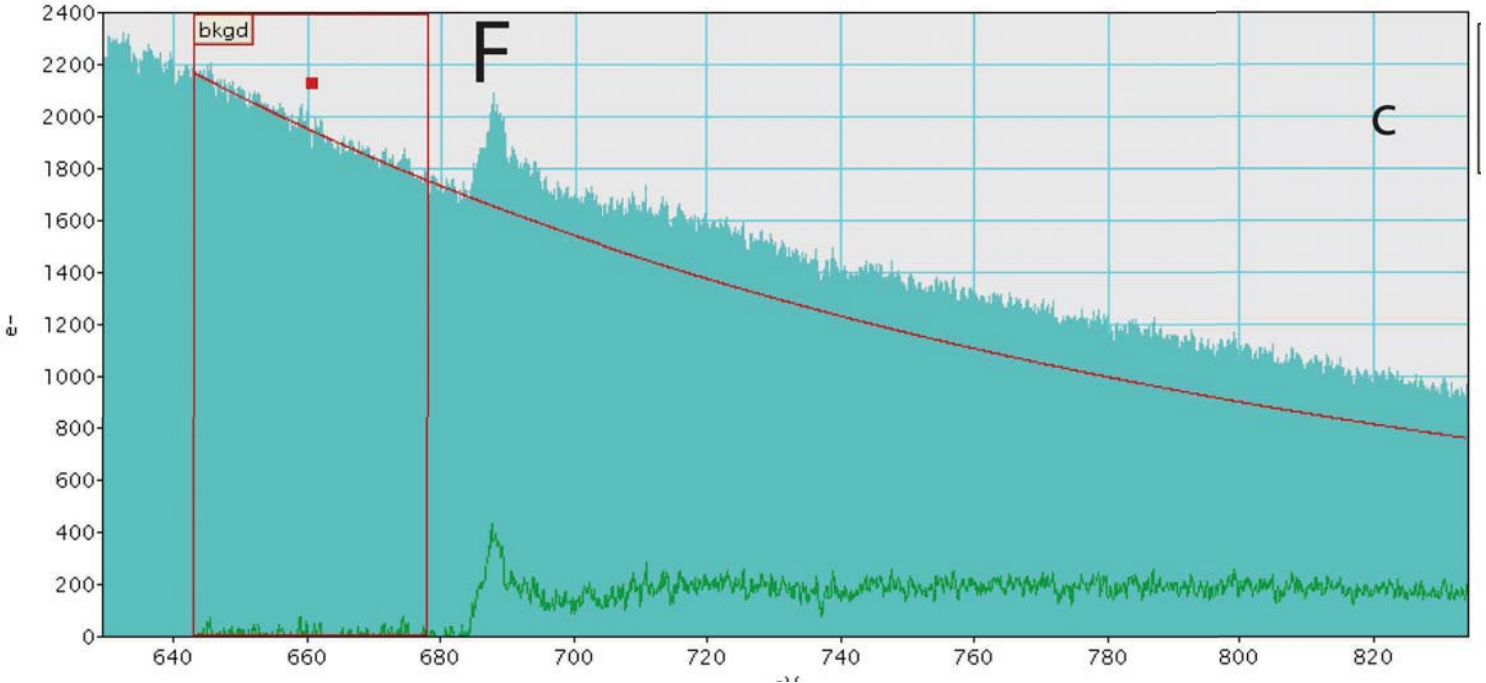
bkgd
F
c
e-

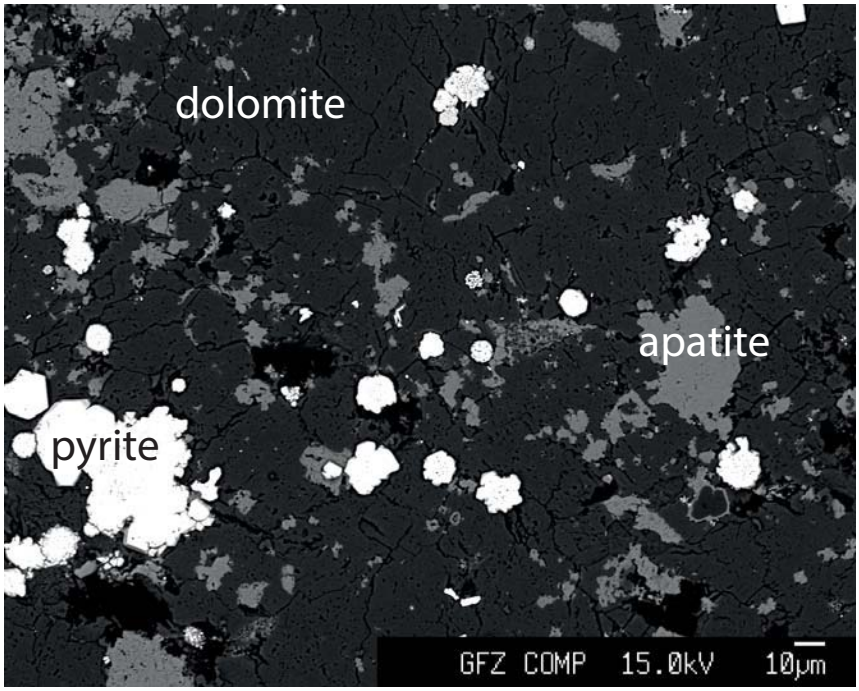
dolomite
apatite
pyrite
GFZ COMP 15.0kV 10µm

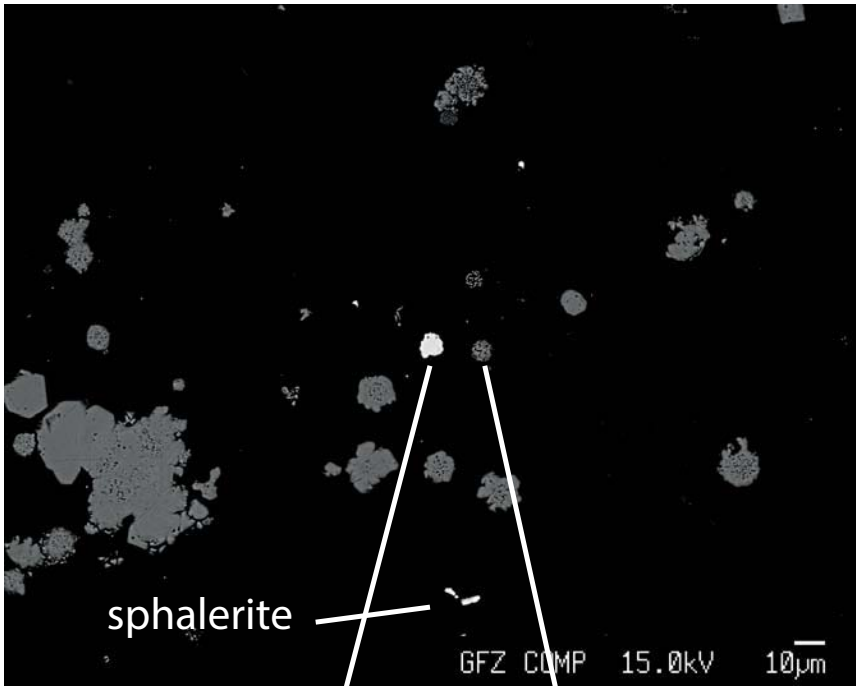
sphalerite
GFZ COMP 15.0kV 10µm

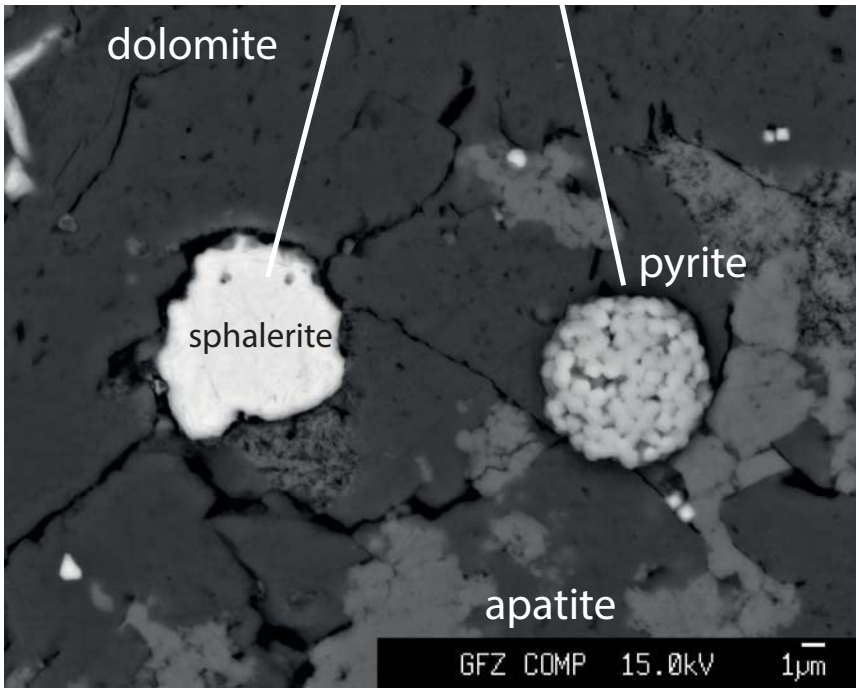
dolomite
pyrite
sphalerite
apatite
GFZ COMP 15.0kV 1µm

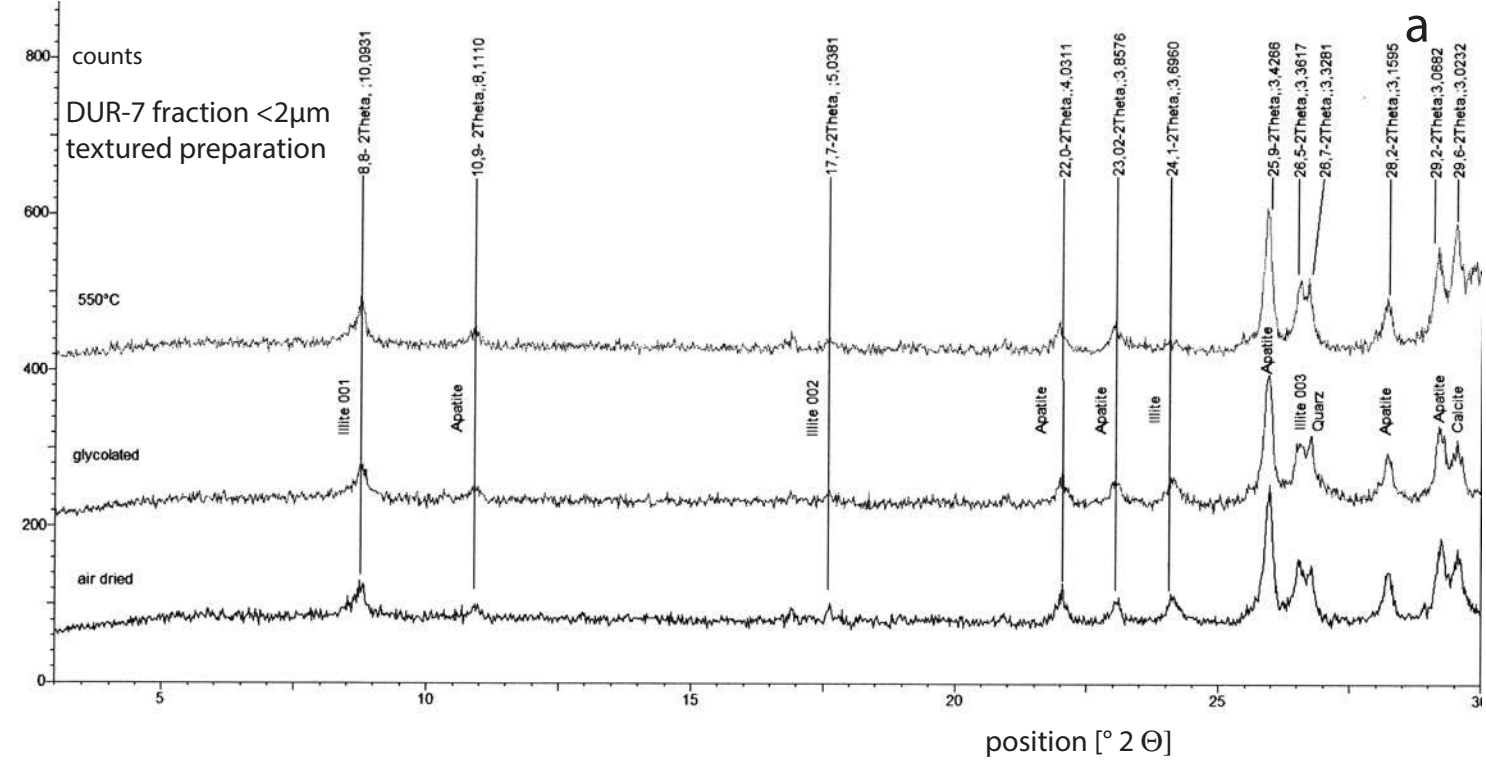
a
counts
DUR-7 fraction <2µm
textured preparation
550°C
glycolated
air dried
8,8- 2Theta,;10,0931
10,9- 2Theta,;8,1110
17,7-2Theta,;5,0381
22,0-2Theta,;4,0311
23,02-2Theta,;3,8576
24,1-2Theta,;3,6960
25,9-2Theta,;3,4266
26,5-2Theta,;3,3617
26,7-2Theta,;3,3281
28,2-2Theta,;3,1595
29,2-2Theta,;3,0682
29,6-2Theta,;3,0232
illite 001
Apatite
illite 002
Apatite
Apatite
illite
Apatite
illite 003
Quarz
Apatite
Apatite
Calcite
position [° 2 Θ]

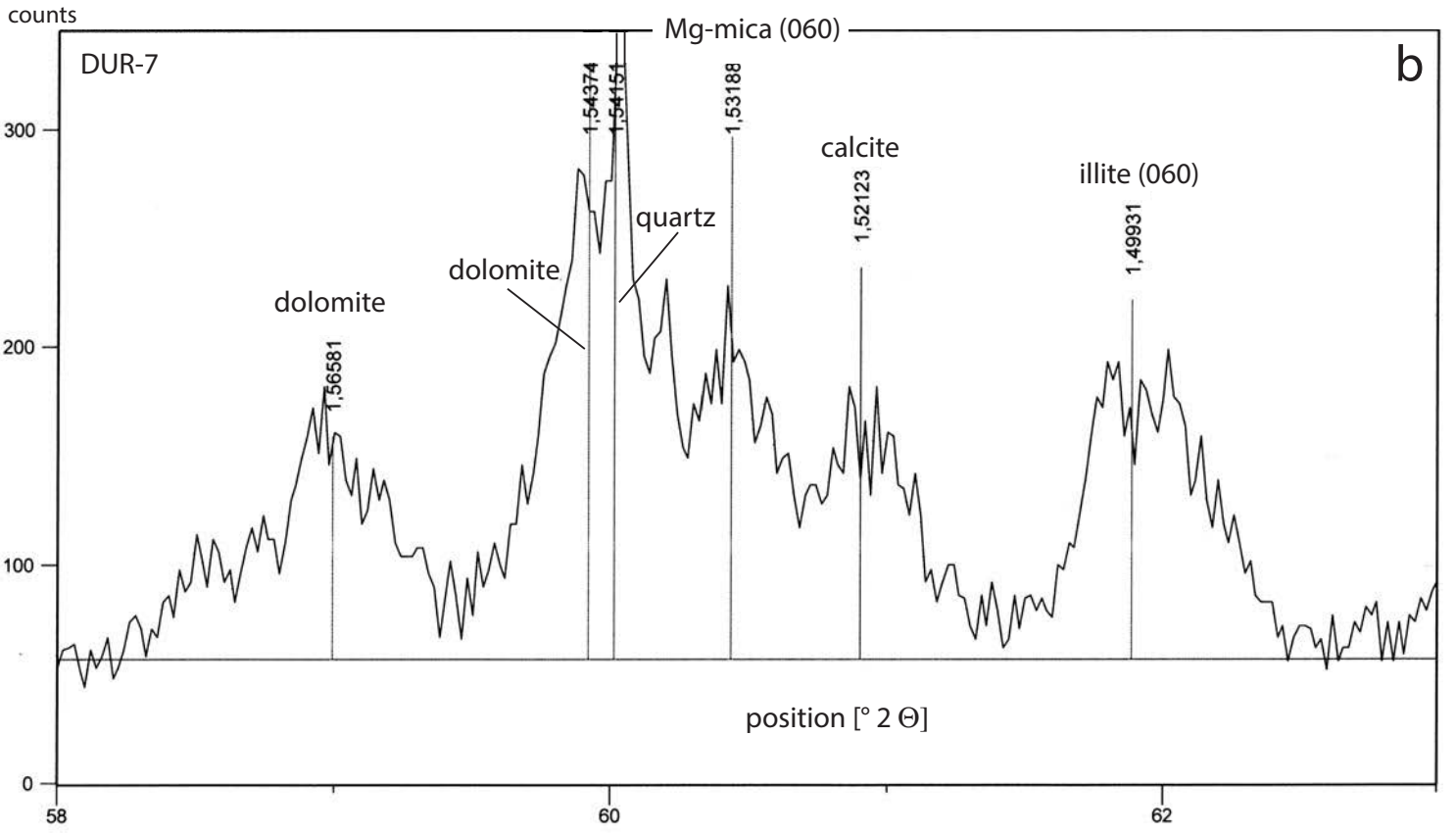
counts
DUR-7
b
Mg-mica (060)
1,54374
1,54151
1,53188
calcite
1,52123
illite (060)
1,49931
quartz
dolomite
dolomite
1,56581
position [° 2 Θ]

Table 1 Electron microprobe analysis of fluorophlogopite and illite from phosphorite/Tal Group, calculated on the basis of 22 oxygen; OH = 4-F; DUR-7: WDS data, DUR11, DUR15, MA-4 by EDS, normalized to 100 wt%

	fluorophlogopite sample DUR-7											
wt%/no.	6	7	8	13	14	23	24	28	29	30	31	33
P_2O_5	0.15	0.09	0.12	0.09	0.14	0.25	0.13	0.04	0.09	0.16	0.09	0.20
SiO_2	46.03	47.07	46.45	46.75	46.85	46.14	47.38	46.73	46.70	48.10	46.40	46.40
Al_2O_3	11.21	11.16	11.21	10.79	10.93	11.39	11.27	11.30	11.09	9.80	11.31	11.16
V_2O_3	0.44	0.33	0.29	0.37	0.29	0.30	0.47	0.33	0.35	0.17	0.38	0.15
FeO_{tot}	0.06	0.00	0.06	0.00	0.00	0.00	0.18	0.21	0.00	0.53	0.01	0.28
MgO	28.12	28.11	28.16	28.28	28.21	28.07	27.53	28.67	28.22	28.50	28.50	28.44
MnO	0.04	0.00	0.00	0.00	0.00	0.22	0.00	0.19	0.00	0.00	0.00	0.00
CaO	0.44	0.41	0.41	0.37	0.41	0.48	0.41	0.11	0.29	0.56	0.43	0.52
Na_2O	0.03	0.03	0.01	0.04	0.03	0.02	0.00	0.04	0.05	0.05	0.00	0.05
K_2O	6.38	6.26	6.01	6.10	6.32	6.08	6.55	6.11	6.03	6.11	6.15	6.05
F	6.58	7.09	6.73	6.68	6.77	6.53	6.87	6.68	6.72	6.21	6.52	6.49
Σ (F-corr)	96.70	97.57	96.62	96.66	97.10	96.71	97.90	97.61	96.71	97.57	97.04	97.00
pfu												
P	0.009	0.005	0.007	0.005	0.008	0.014	0.007	0.002	0.005	0.009	0.005	0.011
Si	6.172	6.232	6.207	6.244	6.238	6.178	6.264	6.186	6.229	6.371	6.179	6.190
Al	1.771	1.741	1.765	1.699	1.715	1.797	1.756	1.763	1.743	1.530	1.775	1.755
Σ Tet	7.952	7.978	7.979	7.948	7.962	7.989	8.028	7.952	7.977	7.910	7.959	7.956
V	0.039	0.029	0.026	0.033	0.025	0.026	0.041	0.029	0.031	0.015	0.033	0.013
Mg	5.621	5.548	5.610	5.632	5.600	5.603	5.427	5.659	5.612	5.629	5.659	5.657
Mn	0.005	0.000	0.000	0.000	0.000	0.024	0.000	0.021	0.000	0.000	0.000	0.000
Fe	0.006	0.000	0.006	0.000	0.000	0.000	0.020	0.023	0.000	0.059	0.002	0.031
Σ Oct	5.671	5.578	5.642	5.665	5.626	5.654	5.488	5.732	5.643	5.702	5.693	5.701
Ca	0.063	0.058	0.059	0.052	0.059	0.069	0.058	0.016	0.041	0.080	0.061	0.074
Na	0.008	0.008	0.003	0.010	0.007	0.004	0.000	0.010	0.013	0.013	0.000	0.013
K	1.091	1.057	1.024	1.039	1.074	1.038	1.105	1.032	1.026	1.032	1.045	1.030
Σ Int	1.162	1.124	1.086	1.102	1.140	1.111	1.163	1.058	1.080	1.125	1.106	1.116
F	2.790	2.968	2.844	2.822	2.851	2.765	2.872	2.797	2.834	2.601	2.746	2.738
OH	1.210	1.032	1.156	1.178	1.149	1.235	1.128	1.203	1.166	1.399	1.254	1.262
Σ Kat	14.775	14.674	14.700	14.709	14.719	14.740	14.671	14.740	14.695	14.729	14.753	14.763

Table 1 continued

	fluorophlogopite sample DUR-7									Dur-11	DUR-15	MA-4
wt%/no.	34	36	37	47	48	49	50	51	average	7	1	26
P_2O_5	0.31	0.11	0.11	0.04	0.00	0.03	0.01	0.02	0.11(08)			
SiO_2	45.43	47.00	46.78	48.89	46.81	47.61	48.53	49.26	47.47(98)	53.77	48.55	52.94
Al_2O_3	11.58	10.98	11.16	9.75	10.48	10.32	9.54	9.18	10.78(70)	8.95	9.36	10.67
V_2O_3	0.13	0.26	0.39	0.24	0.27	0.19	0.14	0.18	0.28(10)			
FeO_{tot}	0.31	0.04	0.00	0.20	0.04	0.14	0.21	0.00	0.11(14)	3.92	0.77	
MgO	28.28	28.44	28.28	28.40	28.45	29.02	28.53	28.86	28.35(31)	26.31	27.64	26.19
MnO	0.12	0.08	0.13	0.00	0.00	0.20	0.02	0.15	0.01(08)			
CaO	0.70	0.40	0.42	0.19	0.25	0.23	0.24	0.30	0.38(14)			
Na_2O	0.09	0.09	0.10	0.00	0.08	0.01	0.01	0.02	0.04(3)			1.12
K_2O	6.43	6.18	6.18	5.76	5.97	5.81	5.86	5.86	6.11(21)	7.03	9.02	5.41
F	6.38	6.62	6.36	5.90	6.22	6.03	6.13	5.79	6.47(34)		7.79	6.10
Σ (F-corr)	97.07	97.41	97.24	96.89	95.96	97.05	96.63	97.18	97.38(45)			
pfu												
P	0.018	0.006	0.006	0.002	0.000	0.002	0.001	0.001	0.006			
Si	6.096	6.234	6.220	6.467	6.282	6.312	6.446	6.500	6.288	6.944	6.380	6.724
Al	1.831	1.717	1.749	1.520	1.658	1.613	1.493	1.428	1.683	1.348	1.450	1.598
Σ Tet	7.945	7.957	7.975	7.990	7.939	7.926	7.940	7.928	7.977	8.292	7.830	8.322
V	0.012	0.022	0.034	0.021	0.024	0.017	0.012	0.016	0.025			
Mg	5.657	5.624	5.606	5.601	5.692	5.736	5.650	5.677	5.599	5.066	5.416	4.960
Mn	0.014	0.009	0.015	0.000	0.000	0.023	0.002	0.017	0.000			
Fe	0.035	0.005	0.000	0.022	0.005	0.016	0.023	0.000	0.012	0.424	0.084	
Σ Oct	5.717	5.661	5.655	5.644	5.721	5.791	5.687	5.710	5.635	5.746	5.500	5.282
Ca	0.100	0.057	0.060	0.027	0.037	0.033	0.034	0.042	0.054			
Na	0.023	0.023	0.026	0.000	0.020	0.003	0.002	0.006	0.010			0.288
K	1.101	1.046	1.048	0.972	1.022	0.983	0.993	0.986	1.032	1.158	1.512	0.876
Σ Int	1.224	1.125	1.135	0.999	1.079	1.018	1.028	1.034	1.097	1.158	1.512	0.964
F	2.707	2.777	2.674	2.468	2.640	2.528	2.575	2.416	2.710		3.238	2.452
OH	1.293	1.223	1.326	1.532	1.360	1.472	1.425	1.584	1.290		0.762	1.548
Σ Kat	14.868	14.737	14.758	14.631	14.739	14.734	14.655	14.671	14.702	14.877	14.842	14.246

Table 1 continued

	illite sample DUR-7											
wt%/no.	1	4	9	21	22	25	26	27	32	35	38	10
P_2O_5	0.12	0.08	0.11	0.12	0.13	0.14	0.01	0.01	0.16	0.05	0.10	0.11
SiO_2	47.73	48.25	47.35	48.09	50.13	49.42	46.54	47.23	49.58	47.67	46.69	52.20
Al_2O_3	32.95	31.21	31.69	30.97	26.50	27.77	37.56	37.68	34.00	35.80	37.27	26.05
V_2O_3	0.11	0.19	0.08	0.08	0.11	0.15	0.12	0.05	0.09	0.20	0.06	2.90
FeO_{tot}	5.68	5.87	6.33	5.44	7.17	6.27	0.84	0.71	2.30	0.90	1.90	0.18
MgO	n.d.	n.d.	1.20	2.06	3.20	3.32	0.89	0.86	1.65	1.68	0.63	4.57
MnO	0.12	0.00	0.19	0.00	0.00	0.12	0.00	0.00	0.00	0.00	0.09	0.00
CaO	0.31	0.40	0.41	0.37	0.48	0.51	0.22	0.18	0.51	0.15	0.20	0.45
Na_2O	0.13	0.14	0.18	0.09	0.05	0.07	1.20	1.23	0.23	0.16	0.41	0.03
K_2O	9.98	10.06	9.82	9.89	9.60	10.07	9.25	8.70	7.41	10.14	10.27	7.03
F	0.17	0.34	0.20	0.31	0.70	0.42	0.03	0.06	0.27	0.00	0.00	1.14
Σ (F-corr)	96.87	96.12	97.12	97.01	97.65	97.84	96.22	96.29	95.78	96.34	97.21	94.24
pfu												
P	0.007	0.005	0.006	0.007	0.007	0.008	0.001	0.001	0.009	0.003	0.006	0.006
Si	6.340	6.472	6.311	6.386	6.675	6.560	6.061	6.113	6.437	6.210	6.074	6.910
Al IV	1.660	1.528	1.689	1.614	1.325	1.440	1.939	1.887	1.563	1.790	1.926	1.090
Σ Tet	5.158	4.934	4.978	4.847	4.159	4.344	5.765	5.748	5.203	5.497	5.715	4.064
Al VI	3.498	3.405	3.289	3.233	2.834	2.904	3.826	3.861	3.640	3.707	3.789	2.975
V	0.009	0.017	0.007	0.007	0.009	0.013	0.011	0.004	0.008	0.017	0.005	0.254
Mg	0.000	0.000	0.238	0.408	535	0.657	0.172	0.167	0.319	0.326	0.122	0.902
Mn	0.013	0.000	0.021	0.000	0.000	0.013	0.000	0.000	0.000	0.000	0.010	0.000
Fe	0.631	0.658	0.706	0.604	0.798	0.696	0.091	0.077	0.250	0.099	0.207	0.020
□ Oct	4.152	4.080	4.260	4.252	4.276	4.283	4.099	4.108	4.216	4.149	4.133	4.151
Ca	0.044	0.058	0.058	0.052	0.069	0.073	0.030	0.025	0.070	0.021	0.028	0.064
Na	0.034	0.038	0.045	0.024	0.013	0.019	0.302	0.308	0.059	0.042	0.104	0.007
K	1.691	1.721	1.670	1.675	1.631	1.705	1.537	1.436	1.227	1.685	1.704	1.187
Σ Int	1.769	1.817	1.773	1.752	1.713	1.796	1.869	1.769	1.357	1.748	1.837	1.258
F	0.069	0.143	0.086	0.131	0.294	0.177	0.011	0.026	0.113	0.000	0.000	0.477
OH	3.931	3.857	3.914	3.869	3.706	3.823	3.989	3.974	3.887	4.000	4.000	3.523
Σ Kat	13.921	13.897	14.033	14.004	13.990	14.080	13.968	13.877	13.573	13.896	13.970	13.409

Table 1 continued

V-illite sample DUR-7

wt%/#	12	20	16	10	11	15	average
P_2O_5	0.11	0.04	0.08	0.11	0.09	0.11	0.09
SiO_2	48.84	48.53	53.45	52.20	52.34	52.01	49.18
Al_2O_3	30.82	34.30	28.79	26.05	25.70	22.58	31.27
V_2O_3	0.56	0.51	2.29	2.90	2.91	5.10	0.91
FeO_{tot}	4.36	2.06	0.00	0.18	0.15	0.00	2.95
MgO	2.18	2.64	3.89	4.57	5.72	9.34	2.58
MnO	0.08	0.00	0.01	0.00	0.00	0.00	0.00
CaO	0.40	0.35	0.35	0.45	0.50	0.35	0.04
Na_2O	0.09	0.13	0.00	0.03	0.00	0.00	0.36
K_2O	9.59	8.46	6.72	7.03	6.61	5.28	0.24
F	0.50	0.48	1.03	1.14	1.41	2.09	8.76
Σ (F-corr)	97.11	97.07	96.18	94.24	95.01	96.44	0.54
pfu							
P	0.006	0.002	0.004	0.006	0.005	0.006	0.005
Si	6.445	6.275	6.863	6.910	6.873	6.798	6.438
Al IV	1.555	1.725	1.137	1.090	1.127	1.202	1.562
A□□□□	4.794	5.228	4.357	4.064	3.978	3.478	4.923
Al VI	3.239	3.503	3.219	2.975	2.851	2.277	3.361
V	0.049	0.043	0.194	0.254	0.252	0.440	0.056
Mg	0.429	0.509	0.745	0.902	1.120	1.820	0.422
Mn	0.009	0.000	0.001	0.000	0.000	0.000	0.004
Fe	0.481	0.223	0.000	0.020	0.017	0.000	0.347
Σ Oct	4.206	4.278	4.160	4.151	4.240	4.537	4.190
Ca	0.056	0.048	0.048	0.064	0.071	0.049	0.051
Na	0.024	0.033	0.000	0.007	0.001	0.000	0.066
K	1.614	1.396	1.101	1.187	1.107	0.880	1.506
Σ Int	1.694	1.477	1.148	1.258	1.179	0.929	1.622
F	0.208	0.194	0.418	0.477	0.586	0.864	0.183
OH	3.792	3.806	3.582	3.523	3.414	3.136	3.817
Σ Kat	13.901	13.755	13.308	13.409	13.419	13.467	13.812

Table 2: Results of ROC-Eval and TOC analysis

sample no.		run no	S1[+)]	S2	S3	T_{max}	HI[**)]	OI[***)]	TOC
				mg/sample		°C	mg/TOC		wt%
DUR 9	phos. mudstone	G013729	0.01	0.01	0.40	405	1	28	1.44
DUR 15a	phos. mudstone	G013730	0.01	0.08	0.25	406	9	29	0.87
DUR 15b	pyrite layer	G013731	0.00	0.04	0.11	337	4	12	0.90
DUR 15Rest	mixed	G013732	0.00	0.02	0.11	407	2	10	1.09
MA 5	phos. mudstone	G013733	0.00	0.01	0.04	337	0	2	2.20
MA 10c	phos. mudstone	G013734	0.00	0.02	0.44	413	3	65	0.67

[+)] for explanation of S1, S2, S3 see text; [**)] HI = hydrogen index; [***)] OI = oxygen index